Advanced Composites and Hybrid Materials (2025) 8:363
https://doi.org/10.1007/s42114-025-01462-3

RESEARCH

Manufacturing a low-carbon geopolymer self-sensing composite for intelligent structure

Dongyu Wang[1,2] · Zuhua Zhang[1] · Siqi Ding[3] · Chaolie Ning[4] · Cheng Shi[4] · Xiaoqing Liu[2] · Qiang Ren[1] · Zhengwu Jiang[1]

Received: 30 May 2025 / Revised: 28 August 2025 / Accepted: 3 September 2025

Abstract

The advancement of smart building and infrastructure has increased the demand for intelligent materials with highly sensitive structural health monitoring (SHM) function. This study reports a high cost-effective strategy of manufacturing geopolymer self-sensing composites (GSCs) with high strength and sensitivity yet low carbon footprint. The effects of the precursor composition and conductive fillers, i.e., nano carbon black (NCB) and copper coated steel fiber (CSF), on the mechanical and electrical properties were investigated. To achieve high and stable sensitivity, the self-sensing behaviors and underlying mechanisms of hybrid NCB and CSF reinforced GSCs were examined through multiscale microstructural analyses. Pore structures were systematically analyzed using nitrogen adsorption desorption (NAD), mercury intrusion porosimetry (MIP), and X-ray computed tomography (X-CT), while interface microstructure was characterized via scanning electron microscopy (SEM), transmission electron microscopy (TEM), and energy-dispersive spectroscopy (EDS). The results indicate that the hybrid NCB and CSF system forms a three-dimensional reinforcing and continuous conductive network within the cross-linked SiO_4 and AlO_4 tetrahedral framework. This synergistic effect significantly enhances the self-sensing performance of GSCs by refining the nanopore structure, improving conductive pathway connectivity, enhancing ductility at low strain levels, and maintaining structural stability under high strain. An optimal GSC mixture composed of 60% ground granulated blast furnace slag, 25% metakaolin, and 15% silica fume manufactured in this study achieved a maximum gauge factor of 3853.4, representing an order-of-magnitude improvement in sensitivity compared to the Portland cement–based counterpart. GSCs demonstrated high potential for SHM application, providing an innovative material manufacturing strategy for next-generation intelligent structure.

Keywords Geopolymer · Self-sensing · Intelligent structure · Structural health monitoring · Flexural loading

1 Introduction

In context of advancement in data-driven and intelligent technologies, smart cities have evolved from a promising concept to a tangible version to resolving the challenges of intense urbanization, high-energy consumption, and greenhouse gas emissions [1–3]. The integration of advanced methods and intelligent elements empowers smart cities to transform conventional passive service building sectors into proactive self-responders. This transformation further facilitates the multifunctionality, sustainability, and cost-effectiveness of infrastructures and buildings [2, 4]. Structural health monitoring (SHM) is one of the most promising and widely applicable technologies for smart infrastructures and buildings, playing a pivotal role in ensuring the safety, robustness, and resilience throughout the entire lifecycle of

✉ Zuhua Zhang
zhangzuhua@tongji.edu.cn

1 Key Laboratory of Advanced Civil Engineering Materials of Ministry of Education, School of Materials Science and Engineering, Tongji University, Shanghai 201804, China

2 State Key Laboratory of Advanced Marine Materials, Ningbo Institute of Materials Technology and Engineering, Chinese Academy of Sciences, Ningbo 315201, China

3 Department of Civil and Environmental Engineering, The Hong Kong Polytechnic University, Hung Hom, Kowloon, Hong Kong, China

4 College of Civil Engineering, Tongji University, Shanghai 201804, China

Published online: 01 October 2025

a building or infrastructure [5]. Current sensing technologies for SHM primarily involve strain gauges, piezoelectric, optical fiber, and magnetoresistive sensors. Nevertheless, most of these sensors face challenges in cost-effectiveness, long-term durability, and great compatibility with cementitious structures [6–9]. The onset and flourishing of self-sensing cementitious composites (SSCCs) are envisioned as a promising solution to address these issues. SSCCs are composed of the cementitious matrix and conductive fillers, and exhibit an electrical signal response to the deformation of conductive networks under external loads [10]. Through monitoring of early deformations and damage as part of a structure, SSCCs can prevent catastrophic failures [11]. As a result, SSCCs not only function as load-bearing elements, but also serve as in situ and real-time sensors for SHM application.

Generally, most SSCCs are manufactured using ordinary Portland cement (OPC), which is an energy and emission intensive product [12, 13]. Attempts to alleviate environmental pressure by utilizing industrial and agricultural by-products have been made to develop greener alternatives. In this regard, geopolymer self-sensing composites (GSCs) characterized by a clinker-free manufacturing process exhibit comparable or even higher early mechanical, durable, multifunctional, and environmental performances compared to SSCCs, making them an appropriate alternative [14]. Geopolymer is synthesized by alkali activation of aluminosilicate precursors derived from industrial by-products, contributing to reduction of carbon emission by 50–70% and energy consumption around 50% [15–17], of course, which depend on specific formulation. Due to the existence of rich alkali metal cations and a large number of gel pores, GSCs fabricated with the optimized precursor composition exhibit excellent electrical and sensing behaviors even without comprising additional conductive fillers [14]. As the cations occupy the voids in the 3D framework consisting of SiO_4 and AlO_4 tetrahedra, the ion migration, charge balance, and local dipoles lead to higher ionic environment in the pore solution [18, 19].

Nevertheless, the composition of GSCs exhibits significant complexity and variability depending on the sources of precursors, the type and modulus of alkaline activator, as well as the type and contents of conductive fillers. These factors, especially the varying precursors, pose challenges in clearly understanding how complex chemical compositions affect the microstructural, engineering, and multifunctional performance of GSCs [20, 21]. For example, the variation of silica (Si), alumina (Al), and calcium (Ca) concentrations of precursor determinates the evolution of geopolymerization products in GSCs. Calcium (alumina) silicate hydrate (C-(A)-S–H) gel is the primary product in rich-Ca geopolymer (typically for ground granulated blast furnace slag (GGBFS)-based composites), which determines the dense microstructure and mechanical strength [22]. As for fly ash (FA) or metakaolin (MK)-based geopolymers, their products are mainly composed of sodium/potassium aluminosilicate hydrate (N/K-A-S–H) gel with inferior space-filling capability than that of C-(A)-S–H [17]. The denser and more compact structure with refined mesopores facilitates the connectivity of conductive paths, thereby improving the electrical and sensing performance of GSCs [23]. As reported in a previous study, the utilization of 25% silica fume (SF) increases 14.8% total porosity with a large number of mesopores (< 10 nm), leading to high electrical conductivity and enhanced sensing sensitivity, while the addition of MK induces coarse pores with diameter greater than 200 nm, resulting in poor conductive networking and relatively lower strength [24]. Besides, the metalogical components of precursor are also critical for GSCs. GGBFS contains metallic iron microparticles could be acted as a conductive microfiller to enhance the electrical properties. GGBFS-based GSC presents sufficient self-sensing properties even without conductive fillers, and the electrical resistivity is one order of magnitude lower than that of OPC-based SSCCs at the frequency of 40 Hz [25]. However, GGBFS exhibits a higher geopolymerization degree at early ages, with C-(A)-S–H combining water into the gel [24]. This reduces moisture content and electrical conductivity, potentially leading to lower sensing repeatability. Conversely, the geopolymerization of MK results in less free water consumption, promoting ion migration and higher early-age electrical conductivity [24, 26].

Based on the intrinsic advantages on self-sensing property, GSCs have attracted widespread attention for the potential in SHM. It has been proven that choosing proper conductive filler(s) is crucial for obtaining high sensitivity of GSC and high sensing stability over time [24], yet systematic investigations in this domain remain scare. Saafi et al. [27] first demonstrated the self-sensing properties of fly ash–based GSC containing in situ reduced graphene oxide (rGO), reporting a conductivity enhancement from 0.77 to 2.38 Sm^{-1} as rGO content increased from 0 to 0.35 wt.%. The latest study [19] revealed that adding nano carbon black (NCB) into GSCs could enhance the sensitivity and stability through the rearrangement of NCB and reconstruction of conductive fillers under loading. However, these single microscale or nanoscale carbon-based filers exhibit impact on mechanical properties, making it difficult to meet the requirements of structural engineering for high load-bearing capacity and durability. Because of this problem, the incorporation of steel fibers remains an effective approach that enhances the mechanical strength and toughness of cementitious matrices by fiber debonding, bridging, and pull-out effects [28]. With sufficient deformation capacity (rather than abrupt fracture) under loading, it is able to build up the relationship between electrical resistance signal and crack opening displacement, i.e., monitoring the structural damage

extent [29]. While current research primarily focuses on the optimization of individual properties, such as mechanical performance, electrical conductivity, or sensing sensitivity, there is limited research on GSCs comprehensively considering sensitivity, stability, and toughness. In particular, the synergistic multi-scale strengthening and toughening effects, conductive and sensing behaviors, and correspondingly underlying mechanisms between macro-scale steel fibers and nano-scale conductive fillers within geopolymer matrices have not yet been elucidated so far.

This study aims to investigate the synergistic enhancement effects and mechanisms of mechanical, electrical, and self-sensing properties in GSCs by constructing a conductive system incorporating hybrid CSF and NCB. It focuses particularly on the evolution of pore structure and interface microstructure under flexural load, the effect of dispersion, and alignment of CSF and NCB. In addition to an in-depth analysis of the self-sensing mechanism, it also gives ecological and economic assessments for various formulations. Based on these results, a low-carbon and cost-effective GSC manufacturing strategy is proposed, while critical challenges and future development pathways are discussed.

2 Experimental procedures

2.1 Raw materials

The GSC specimens were mainly prepared using GGBFS (Jiyuan Guotai Micro Powder Technology Co., Ltd.), MK (Inner Mongolia Super New Material Co., Ltd), and SF (Shanghai Topken Silicon Powder Material Co., Ltd) as precursors. Their physical and chemical properties are given in Table 1. The activator was prepared by potassium hydroxide flake (PH, i.e., KOH, 95% purity; Shanghai Macklin Biochemical Technology Co., Ltd.), potassium silicate powder (PS, i.e., $K_2O{\cdot}3.3SiO_2$; Shanghai Macklin Biochemical Technology Co., Ltd.), and water. The quartz sand with a diameter in the range of 0.1–1.0 mm was used as aggregate. To enhance the electrical and mechanical properties of GSC, NCB with a diameter in the range of 28–30 nm and CSFs in straight and hooked-end shapes with a diameter of 0.2 mm and a length of 13 mm were employed. The dispersant of polyvinylpyrrolidone (PVP, 1 wt.% of precursors) and defoamer of tributyl phosphate (TBP, 0.2 wt.% of precursors) were used to improve NCB dispersion.

2.2 Specimen preparation

The mix proportions are shown in Table 2, wherein the specimens were labeled based on their composition: S01–S04 had different precursor compositions without conductive fillers, CB1–CB4 had different precursor compositions with constant dose of 5.0 wt.% NCB, while SL3/SH3 and SC3 were composed of 60% GGBFS, 25% MK, and 15% SF, and 2 vol.% straight/hooked-end CSFs and hybrid NCB and straight CSFs, respectively. The water-to-binder (w/b) ratio and sand-to-binder (s/b) Ratio of each specimen were kept at 0.42 and 1.0, respectively. The alkaline activator was prepared 24 h prior to specimen preparation by dissolving PH flake and PS powder in water. For NCB-modified alkaline activator, PVP, TBP, and NCB were uniformly dispersed in the pre-prepared alkaline activator following our previous work [19] to ensure homogeneous dispersion of NCB.

Table 1 Physical and chemical properties of the precursors in GSCs

Characterization		GGBFS	MK	SF
Specific surface area (m^2/kg)		428.0	16,953.7	15,738.4
Apparent density (g/cm^3)		2.839	2.515	2.153
Average mean particle size d_{50} (μm)		9.57	4.63	0.79
Chemical composition (%)	Al_2O_3	16.55	49.11	0.82
	SiO_2	32.09	47.19	97.42
	Na_2O	0.40	0.07	0.00
	MgO	8.76	0.51	0.50
	K_2O	0.43	0.16	0.28
	CaO	37.65	0.30	0.25
	MnO	0.32	0.00	0.00
	Fe_2O_3	0.35	0.79	0.10
	P_2O_5	0.00	0.14	0.00
	SO_3	2.60	0.12	0.62
	TiO_2	0.60	1.26	0.00
	LOI	0.25	0.35	0.01

The GGBFS, MK, and SF powders were dry mixed using a cement mortar mixer stirring at a low speed (140 ± 5 r/min) for 2 min, then mixed with alkaline activator (or NCB-modified alkaline activator) by stirring at a low speed for 1 min and followed by a high speed (285 ± 10 r/min) for 30 s. During the initial 1-min low-speed stirring after quartz sand addition, CSFs were gradually added, followed by high-speed stirring for 1 min to ensure homogeneity. The fresh mixtures were cast in 40 mm × 40 mm × 160-mm steel molds, wherein two stainless steel electrodes were embedded parallel to the longitudinal axis and placed 10 mm from the specimen ends. Following casting, the specimens were sealed with plastic film and cured under laboratory environment for 24 h. After demolding, the specimens were subsequently cured in a controlled environment at 20 ± 3 ℃ and relative humidity of 65% for 27 days.

2.3 Methodology

During the initial preparation phase, the physical properties of precursors were predetermined. The specific surface area was measure by nitrogen adsorption using a

Table 2 Mixture proportions of GSCs

Specimens	GGBFS (wt.%)	MK (wt.%)	SF (wt.%)	CaO/SiO_2	CaO/Al_2O_3	SiO_2/Al_2O_3	Sand (wt.%)	Activator (wt.%)	Filler type	Filler content
S01	60	35	5	0.56	0.75	1.33	100	42	–	–
S02	60	30	10	0.53	0.75	1.54	100	42	–	–
S03	60	25	15	0.50	0.75	1.78	100	42	–	–
S04	60	20	20	0.47	0.75	2.07	100	42	–	–
CB1	60	35	5	0.56	0.75	1.33	100	42	NCB	5.0 wt.%
CB2	60	30	10	0.53	0.81	1.54	100	42		5.0 wt.%
CB3	60	25	15	0.50	0.81	1.78	100	42		5.0 wt.%
CB4	60	20	20	0.47	0.81	2.07	100	42		5.0 wt.%
SL3	60	25	15	0.50	0.81	1.78	100	42	Straight CSFs	2 vol.%
SH3	60	25	15	0.50	0.81	1.78	100	42	Hooked-end CSFs	2 vol.%
SC3	60	25	15	0.50	0.89	1.78	100	42	Hybrid NCB + straight CSFs	5.0 wt.% NCB + 2 vol.% CSFs

Brunauer–Emmett–Teller analyzer (Micromeritics ASAP 2460, USA). The average mean particle size was determined using laser scattering particle analyzer (Microtrac S3500, USA). Chemical compositions were analyzed by energy dispersive X-ray fluorescence spectrometer (Bruker S2 PUMA, Germany). The apparent density was tested using a Le Chatelier flask with anhydrous kerosene as the displacement medium in accordance with Chinese national standard GB/T 208–2014 [30].

Before testing mechanical strength and sensitivity, all specimens were placed in a vacuum chamber at 40 °C for pre-drying for 7 days to eliminate the possible effect of humidity change on the electrical-based properties of the cementitious composites [31]. The mechanical performances of GSCs were evaluated using a universal mechanical testing system (MTS CMT5305, USA). Specifically, flexural test was carried on three prismatic specimens (40 mm × 40 mm × 160 mm) at a constant loading rate of 0.5 mm/min, while compressive strength was determined on six cubic specimens (40 mm × 40 mm × 40 mm) at 1.2 mm/min. To evaluate the electrical properties, the alternating current (AC) electrical resistance on three specimens were measured at 3, 7, 21, and 28 days using an inductance–capacitance–resistance meter (TH2840A, China), respectively. Besides, the electrochemical impedance spectroscopy (EIS) was measured by a two-probe method using an electrochemical workstation (CS350H, China) in a frequency range from 0.01 Hz to 1 MHz and a low-amplitude AC excitation of 20 mV. The EIS results were analyzed using the equivalent circuit method with ZSimpWin software. The self-sensing properties under flexure were tested using the MTS instrument, with real-time strain and direct current (DC) resistance measured simultaneously. Notably, DC resistances were collected using the digital multimeter (Tektronix DMM6500, USA) after achieving a relatively stable value to minimize the polarization effect [32]. Prior to testing, a strain gauge was attached to the center of the opposite sides of the loading surface, and a dynamic data logger (DH 2820, China) with a sampling frequency of 2 Hz was used to capture strain. The test setup of GSCs under flexural loading can be seen in Fig. A1.

To elucidate the microstructural features of GSCs, selected samples were analyzed by scanning electron microscopy (SEM), transmission electron microscope (TEM), mercury intrusion porosimetry (MIP), nitrogen adsorption desorption (NAD), and X-ray computed tomography (X-CT). SEM (ZEISS Sigma 300VP, Germany) coupled with energy-dispersive spectroscopy (SEM–EDS) analysis for selected areas was performed using the secondary electron model at an operating voltage of 3 kV to investigate the morphologies of geopolymerization products. SEM in backscattered electron (BSE) mode at an operating voltage of 15 kV and TEM-EDS (JEOL JEM 2100, Japan) at an accelerating voltage of 200 kV were used to characterize the interface and geopolymerization products of CSF reinforced GSCs, respectively. The pore structure of the specimens was analyzed by MIP and NAD, following the methodology described in our previous work [19]. A CT scan was performed using an X-ray CT system (GE-Phoenix V |tome |x m, Germany) at 190 kV and 0.45 mA with a minimum pixel resolution of 0.1 mm to investigate the 3D distribution of pores and CSFs within GSCs.

3 Results

3.1 Development of high-strength high-conductivity geopolymer

3.1.1 Effects of precursors on mechanical and electrical properties

Four GSCs without additional conductive fillers (i.e., S01, S02, S03, S04) were fabricated with distinct precursor compositions. The effects of chemical oxide ratios on their mechanical and electrical properties are depicted in Fig. 1. As shown in Fig. 1a, GSC samples achieve high compressive strength of 70 to 80 MPa. Owing to the physical filling effect and pozzolanic reaction of SF [33], the compressive strengths of S02, S03, and S04 with the increase of silica fume content in the precursor increase by 6.7 MPa/9.45%, 6.7 MPa/9.45%, and 5.6 MPa/7.76% compared to S01, respectively. These strength values are even higher than that reported in [29] for samples containing CSF. This indicates that the precursor composition ratio is a critical factor for manufacturing high-strength GSCs. Previous studies have proved that the addition of GGBFS into GSCs provides rich CaO and low-polymerizing SiO_4 tetrahedra, enhancing the geopolymerization and gelation process, resulting in the formation of C-A-S–H gels [19, 34]. However, the precursor containing rich SiO_2 or Al_2O_3 also plays a significant role in the reaction degree, geopolymerization products, and consequent strength.

Herein, the optimal aluminosilicate precursor ratio for GSCs is achieved when the content of MK and SF account for 25–30% and 10–25%, respectively. As for the influence of chemical oxide ratios shown in Fig. 1b–d, the compressive strength of GSCs increases slowly and then decreases with rising CaO/SiO_2 ratio, and it exhibits an initial increase followed by stabilization with increasing CaO/Al_2O_3 and SiO_2/Al_2O_3 ratios because the formation of C-(A)-S–H contributes to high strength and Si–O-Si bond exhibits higher strength than that of Si–O-Al [35]. In contrast to compressive strength, the flexural strength in Fig. 1f–g initially increases rapidly but then gradually decreases with increasing CaO/SiO_2, CaO/Al_2O_3, and SiO_2/Al_2O_3 ratios for limited reaction at high Si/Al ratio [35]. Consequently, the mechanical strength of GSCs reaches relative higher values when the bulk ratios of CaO/SiO_2, CaO/Al_2O_3, and SiO_2/Al_2O_3 are in the rangeof 0.49–0.53, 0.80–0.90, and 1.50–1.80, respectively. As depicted in Fig. 1a and e, S03 with a composition of 60% GGBFS, 25% MK, and 15% SF presents the highest compressive strength of 80.1 MPa and flexural strength of 6.0 MPa, respectively.

As seen in Fig. 1i, AC resistivities of 28-day GSCs at the frequency of 500 kHz are in a range of 5.74 to 13.9×10^4 kΩ·m, which are several orders of magnitude lower than that of SSCCs [31]. Unlike SSCCs, GSCs have high alkali concentrations and numerous nanogel pores within the matrix, resulting in intrinsic electrical properties even without conductive fillers [24, 36]. Wherein, the ionic conduction contributes to the conductive mechanisms, which is determined by the precursor compositions and geopolymerization degree. In Fig. 1g–l, S01 obtains the minimum electrical resistance with the highest CaO/SiO_2 ratio and the lowest CaO/Al_2O_3 and SiO_2/Al_2O_3 ratios, suggesting the significance of CaO and Al_2O_3 contents for high conductivity. Despite the electrical contribution of Ca^{2+} in C-A-S–H, the high CaO concentration will lead to more mobile cations, including K^+ and Ca^{2+}. The presence of Al involves IV-, V-, and VI-coordination states, and the high coordination status may also contribute to the high conductivity due the local dipole enhancement at molecular level [37].

3.1.2 Effects of NCB on mechanical and electrical properties

Figure 2 illustrates the mechanical and electrical properties of GSCs containing NCB. The addition of NCB induces a significant reduction on the mechanical strength. Specifically, the compressive strengths of all the specimens decrease to 65 MPa while the flexural strengths decrease progressively as the mass proportion of MK reduces and SF increases. Compared to other specimens, CB3 exhibits the largest reduction in compressive and flexural strength by 21.0 and 27.1%, respectively. This can be attributed to the instinct porous characteristics and potential agglomeration defects of NCB [38]. Overall, however, the compressive and flexural strengths of the GSCs are still satisfying for most cases of structural application.

NCB with the merits of high conductivity and low cost has been widely accepted as a promising conductive filler to enhance the electrically conductive properties [39]. The introduction of NCB reduces the 28-day electrical resistance of GSCs by an order of magnitude. Their electrical resistance initially increases with the extension of the curing age but declines substantially at the curing age of 21 days, followed by an increase to 28 days. In this process, the resistivities of GSCs increase with the extension of curing ages due to the progress of polymerization and the absence of free water [24]. The lower reactivity of MK, compared to GGBFS, results in less water consumption during the early curing stages [40]. CB1 demonstrated the best strength and conductivity, making it a promising candidate for manufacturing self-sensing binder with structural property requirements. It is worthwhile that NCB has the best modification effect on CB3 with 28-day electrical conductivity enhanced

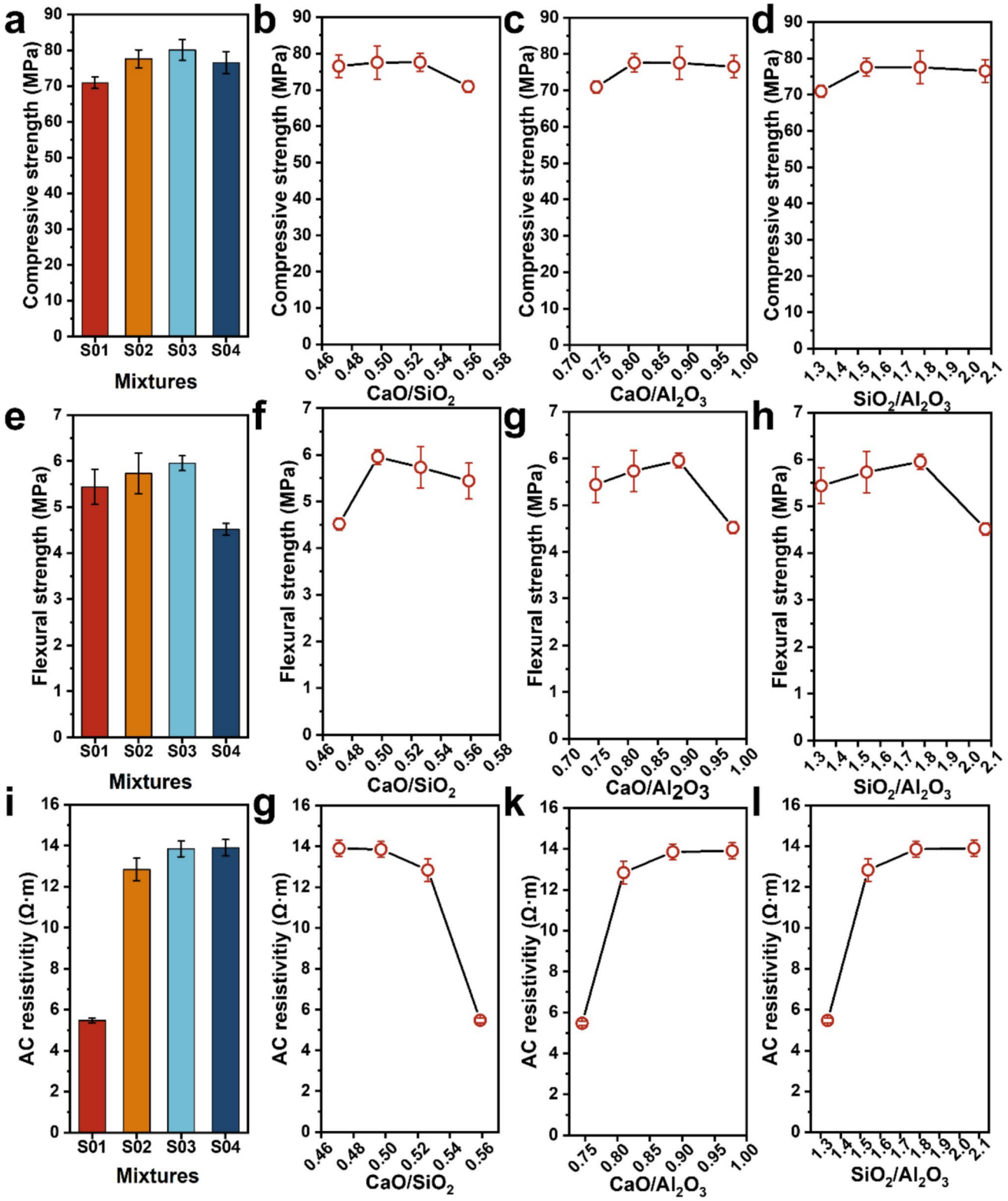

Fig. 1 Effects of precursor compositions on mechanical strength and electrical conductivity of GSCs without conductive fillers at 28 days: (a–d) compressive strength; (e–h) flexural strength; (i–l) AC resistivity

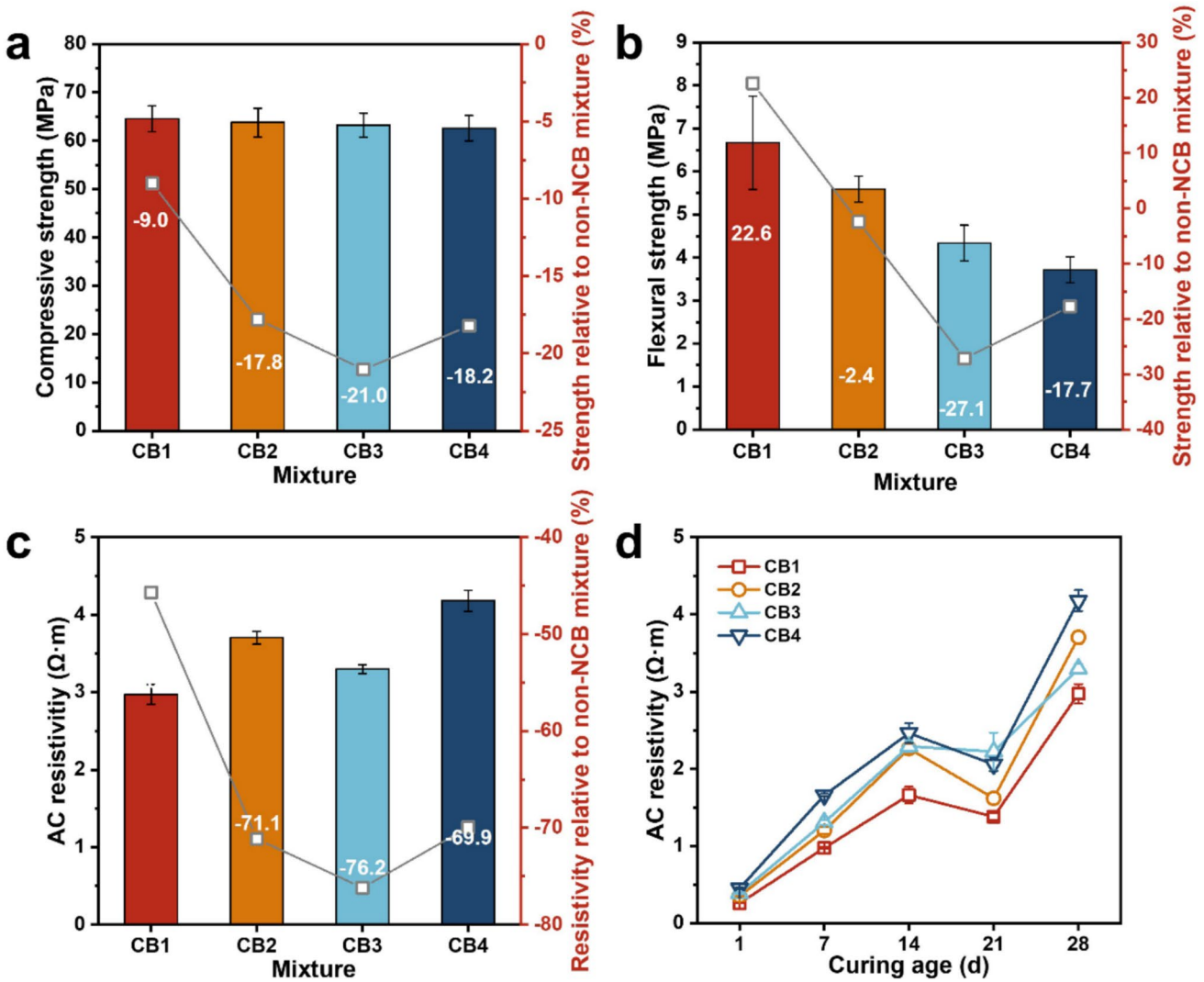

Fig. 2 Effects of NCB on mechanical strength and electrical conductivity of GSCs: (a) compressive strength; (b) flexural strength; (c) 28-day AC resistivity; (d) age dependence of AC resistivity

for 76.2%. However, it faces a common issue of the balance between mechanical strength and electricity-based multifunctionality.

3.1.3 Effects of CSFs on mechanical and electrical properties

CSF is regarded as a promising candidate to address the aforementioned balance issue between strength and conductivity. Based on the two mixtures of S03 and CB3, the effects of CSF addition on the mechanical and electrical properties can be seen in Fig. 3. The compressive strength of GSCs is enhanced, especially for SH3 and SL3, which shows that the hook-end CSF is better than the straight CSF. In comparison to S03, their strengths increase by 27.7 and 21.4%, respectively, at the dose of 2%. The addition of hybrid CSF and NCB enhances the compressive strength to a value similar to S03, it notably improves the strength by 25.5% relative to CB3.

It is clear in Fig. 3b that the flexural toughness of CB3 is higher than that of S03, which is probably due to the nanosized influence of NCB, filling voids and pores within the matrix and embedding in geopolymerization products as C-(A)-S–H nucleation sites, thereby refining the microstructure and improving ductility [41]. However, their quasi-brittle behavior results in the relatively low flexural strength (Fig. 3b, c). Both S03 and CB3 present typical brittle fracture characteristics as the flexural loading reached up to the peak load [19, 42].

The incorporation of CSFs provides an effective solution by improving the flexural peak load and toughness of GSCs due to their high tensile strength and bridging

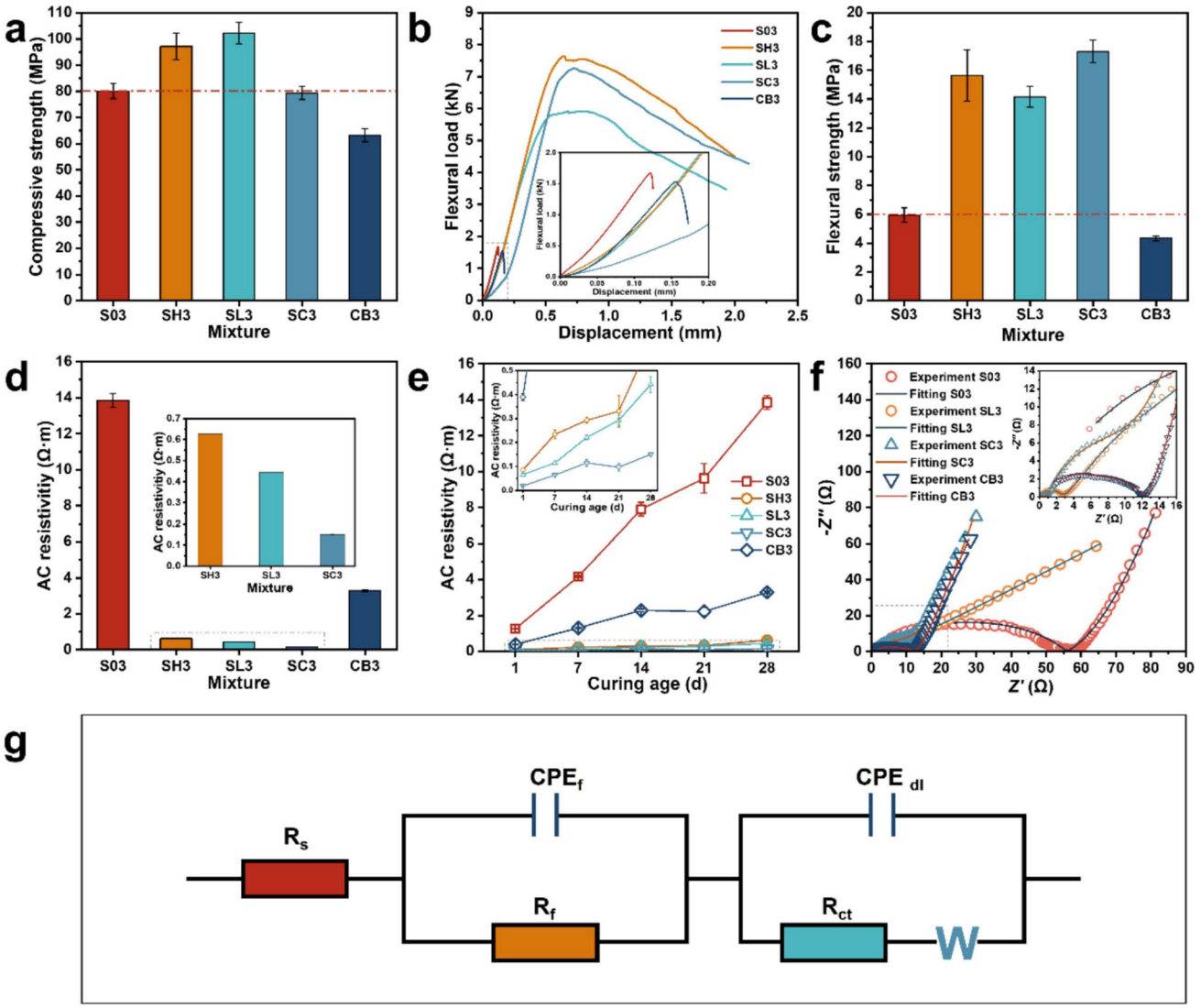

Fig. 3 Effects of single/hybrid CSFs and NCB on mechanical and electrical properties of GSCs containing 60% GGBFS, 25% MK, and 15% SF: (a) compressive strength; (b) flexural load–displacement curves; (c) flexural strength; (d) 28-day AC resistivity; (e) age-dependent AC resistivity; (f) Nyquist plots; (g) equivalent electrical circuit proposed for EIS fitting

effect (Fig. 3b). The fracture energy dissipation and crack deflection and bifurcation via fiber debonding, pull-out, and deflection account for enhancing their fracture toughness [43]. Besides, the mechanical behaviors of GSCs are also determined by their microstructure characterization, which will be discussed in Sects. 3.3 and 4.2. Compared to straight CSF, end-hooked CSF demonstrates superior pull-out resistance due to its higher fiber aspect ratio and enlarged fiber–matrix interfacial bonding area [44], leading to higher flexural strength and toughness of SH3 compared to SL3. Crack propagation under flexural loadings generally covers multiple length scales from microscopic to macroscopic dimensions [45]. The synergistic combination of nanoscale NCB and microscale-diameter CSF enables multiscale reinforcement, with SC3 obtaining the highest flexural strength. This induces a supra-additive reinforcement effect, with strength increases of 85.0% for S03, 10.4% for SL3, 23.3% for SH3, and 289.5% for CB3, respectively.

As seen in Fig. 3d, the addition of end-hooked and straight CSFs induces lower resistivity of the specimens comparing with that of NCB. The 28-day AC resistivities of SH3 (625.9 Ω·m) and SL3 (442.7 Ω·m) are two and three orders of magnitude lower than those of S03 and CB3, respectively. SC3 showed the highest electrical conductivity of 150.6 Ω·m among all specimens, demonstrating that the hybrid addition of NCB and CSF effectively improved electrical performance. Its resistivity shows relatively stable growth with increasing curing age due to the formation of interconnected conductive paths composed of NCB and CSF (Fig. 3e). The Nyquist plots in Fig. 3f reveal a significant

reduction in both the capacitive loop and the impedance modulus upon addition of conductive fillers. SL3 and SC3 exhibit smaller capacitive loops and lower impedance moduli compared to S03 and CB3, particularly in the high-frequency region, indicating faster charge transfer kinetics. SC3 demonstrates an excellent hybrid effect between NCB and CSF, proving the synergistic enhancement of conductivity as Fig. 3d and e depicted.

To further understand the effect of detailed electrochemical parameters on the enhanced electrical characteristics and mechanism, an appropriate equivalent electrical circuit (EEC) was selected based on the previous studies with NCB/CSFs [41, 46, 47] to fit the EIS of GSCs. As illustrated in Fig. 3g, EEC is composed by $R_s(CPE_fR_f)(CPE_{dl}(R_{ct}W))$, where R_s is the solution resistance of GSCs pore solution; CPE_f and R_f in the high-frequency circuit represent the double layer capacitance and resistance of conductive fillers/matrix/fillers structure [41], respectively; CPE_{dl} and R_{ct} in the high-frequency circuit represent double layer capacitance generated at the pore wall/solution interface and charge transfer resistance [48], respectively; W is the Warburg diffusion impedance in the low-frequency region, as expressed in Eq. (1). It should be noted that CPE_f and CPE_{dl} are the constant phase element (CPE), which could be expressed as Eq. (2) [49, 50]:

$$Z_W = \frac{\sigma}{\sqrt{\omega}} - j\frac{\sigma}{\sqrt{\omega}} \tag{1}$$

$$Z_{CPE} = \frac{1}{Q(j\omega)^n} \tag{2}$$

where Z_W is Warburg impedance ($\Omega\cdot cm^2$), σ is Warburg coefficient, Z_{CPE} is the impedance of CPE ($\Omega\cdot cm^2$), Q (Q_f for CPE_f and Q_{dl} for CPE_{dl}) is the admittance of CPE ($\Omega^{-1}\cdot cm^{-2}\cdot s^n$), j is the imaginary, ω is the angular frequency ($rad\cdot s^{-1}$), and n (n_f for CPE_f and n_{dl} for CPE_{dl}) is the phenomenological coefficient. When $n=1$, CPE serves as an ideal double layer capacitor; when $n=0$, CPE serves as a pure resistor; and when $n=0.5$, CPE represents the diffusion-controlled Warburg impedance.

The consequent fitting results of EIS data are summarized in Table 3. The values of R_s exhibit slight increase or nearly unchanged; the values of R_f and R_{ct} significantly decrease, especially for SL3 and SC3, which are reduced by an order of magnitude; Q_f shows a reduction as single/hybrid NCB and CSF are added; and Q_{dl} presents an increasing trend, especially for GSCs containing NCB. The increase in R_s could be attributed to the refined nanopore structure introduced by adding NCB, while the increase in R_s for SL3 may result from the introduction of large pores along with CSF, thus interrupting the original ion transport path within the matrix. Moreover, the reconstruction and modification of conductive networks contribute to the decrease in Q_f as single/hybrid NCB and CSF are added. However, the incorporation of conductive fillers induces numerous tiny double layers with high specific capacitance within the matrix and modifies the capacitance characterization at the pore wall/solution interface, resulting in the growth in Q_{dl} [41, 51].

3.2 Self-sensing assessment of GSCs

Figure 4a–c present the relationship between the fractional change in electrical resistance (FCR) and flexural strain (FCR-strain) for GSCs under flexural loading. Based on the flexural fracture behaviors, the FCR-strain curves of GSCs can be classified into two categories: (1) brittle failure (GSCs without fillers or with only NCB), characterized by a linear increase stage followed by a nonlinear increase stage; (2) ductile failure (GSCs containing single CSF, hybrid NCB, and CSF), characterized by linear elastic stage, microcrack initiation stage, and macrocrack propagation stage [45]. From Fig. 4a, as flexural strain increases, the FCR of GSCs demonstrates a progressive increase. Herein, S03 exhibits the highest FCR during loading; the other three mixtures attain comparable FCR values at failure. Notably, the addition of NCB significantly enhances the FCR with higher linear slope, especially for CB1 which obtains FCR value of 21.8% at crack initiation and 24.8% at ultimate fracture (Fig. 4b), respectively. This enhancement compared to S01 with the lowest FCR may be caused by the greater interfacial adhesion between NCB and the S01 matrix, as well as the unique NCB filling effect on pores and voids (will be revealed in Sect. 3.3). Regarding CSFs reinforced GSCs, both resilience and ductility are substantially improved,

Table 3 EIS fitting for GSCs containing 60% GGBFS, 25% MK, and 15% SF and single/hybrid CSFs and NCB

	R_s($\Omega\cdot cm^2$)	CPE_f Q_f($10^{-5}\Omega^{-1}\cdot cm^{-2}\cdot s^n$)	n_f	R_f ($k\Omega\cdot cm^2$)	CPE_{dl} Q_{dl}(10^{-5} $\Omega^{-1}\cdot cm^{-2}\cdot s^n$)	n_{dl}	R_{ct} ($k\Omega\cdot cm^2$)	W($\times 10^{-4}$ $\Omega\cdot cm^2$)
S03	12.21	30.52	0.867	4.798	2.27	0.674	55.810	1.16
SL3	16.85	9.67	0.976	0.249	5.27	0.658	2.702	4.65
SC3	12.04	3.58	0.901	0.693	30.70	0.782	9.670	1.31
CB3	21.97	9.59	0.511	0.596	27.15	0.967	12.190	2.85

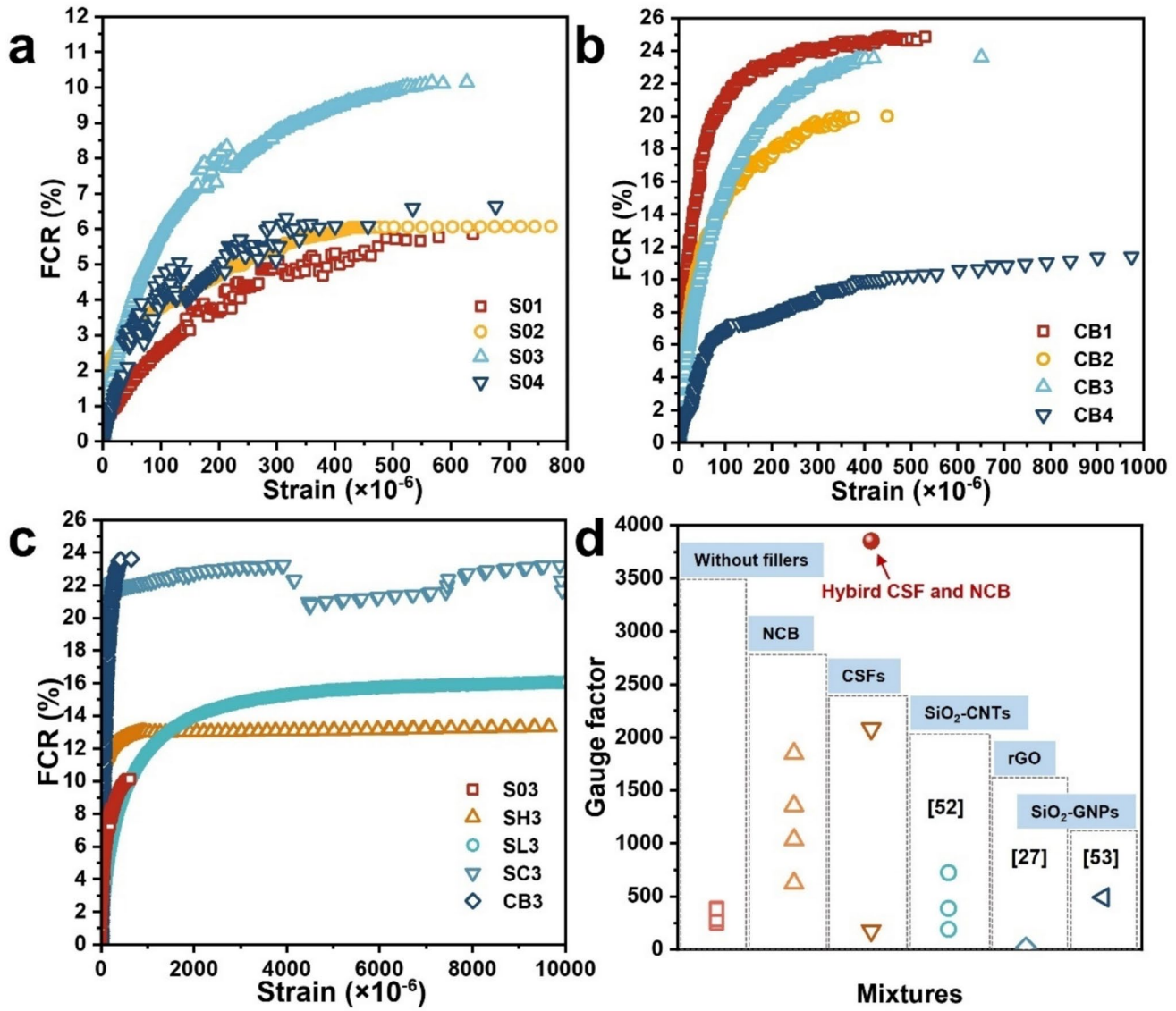

Fig. 4 Self-sensing properties for GSCs under flexural loading: (a) GSCs without conductive fillers; (b) GSCs with NCB; (c) effect of NCB and CSFs on GSCs containing 60% GGBFS, 25% MK, and 15% SF; (d) comparison of *GF* of GSCs (SiO_2-CNTs: SiO_2-coated carbon nanotubes; rGO: in situ reduced graphene oxide; SiO_2-CNTs: SiO_2-coated graphene nanoplatelets) [27, 52, 53]

which directly contribute to enhanced strain-sensing performance under flexural loading (Fig. 4c). Compared to S03, the FCR of SH3, SL3, and SC3 upon initial crack formation are enhanced by 38.5%, 15.7%, and 146.9%, respectively. Under progressive flexural loading, the FCR increases steadily.

Gauge factor (*GF*) is a representative parameter used to characterize the self-sensing properties, which can be obtained by the value of slope in the linear stage of the FCR-strain curves (i.e., $GF=|FCR|/\varepsilon$, where ε is the applied flexural strain). Figure 4d compares the *GF* of GSCs in this work with those reported in relevant literature [27, 52, 53]. GSCs developed in this study exhibit significantly enhanced initial crack detection sensitivity compared to MK-based GSCs [52]. This improvement is further enhanced with NCB incorporation, which achieves a high *GF* value surpassing the previous record value of 724.6 (Fig. 4d). However, CSFs induce an inferior sensitivity in SL3. SH3 exhibits a higher *GF* than that of SL3, which is consistent with the findings of Lu et al. [29]. Considering the findings in Fig. 3c, GSFs modified by NCB exhibit exceptional sensitivity in the low-strain regime while CSF-reinforced GSCs demonstrate significantly enhancement with crack propagation at higher strain levels. The combination of NCB and CSFs enables

synergistic sensitivity improvement across all loading stages. Notably, the *GF* value of 3853.4 in SC3 increases by an order of magnitude compared to S03, showing a strong potential for initial crack monitoring.

3.3 Morphological analysis

3.3.1 Pore structure

Figure 5 illustrates the multiscale pore structure in GSCs as determined by NAD, MIP, and CT techniques. While samples containing different precursor compositions in Fig. 5a exhibit similar adsorption/desorption curve profiles and hysteresis loops types, GSCs with NCB show higher N_2 adsorption volumes than those counterparts without NCB. This observation is further verified by MIP analyses in Table 1, which reveal increased total pore volume and porosity as NCB is added. For example, CB3 exhibits a 17.5% increase alongside a porosity rise from 17.23 to 19.49% when compared to S03. This can be ascribed to the addition of NCB that introduces air voids and porous NCB aggregation, consequently causing its compressive and flexural strengths to decrease by 21.0 and 27.1%, respectively, as depicted in Fig. 2.

Notably, owing to the nano-filling effect of NCB, the average pore diameter and most probable pore diameter of GSCs measured by NAD in Fig. 5d and Table B1 are reduced as it is being added, as quantitatively confirmed by MIP results. The pore refinement arises from the transformation of large pores into small pores, yielding a more continuous and interconnected pore network. This modification directly improves charge transport, as evidenced by a 76.2% reduction in AC resistivity for CB3 compared to S03. In contrast, the addition of CSF substantially increases the pore size diameter in the range from 100 nm to 1 μm, which is probably trapped air voids formed during fabrication [54]. Moreover, hybrid CSFs and NCB could effectively refine the pore structure, particularly reducing macropores. As shown in MIP results of Table B1, the average pore diameter of SC3 is lower than S03 for 11.4%, CB3 for 5.5%, and SL3 for 16.0%, respectively. The characterization and calculation based on X-CT further verify the findings. As demonstrated in Fig. 5 and Table B2, the distribution of pores in SL3 are mainly distributed in the size ranges of 50–100 nm and 100–200 nm, accounting for 26.8 and 37.9%, respectively. Conversely, high amounts of pores in SC3 are concentrated in sizes smaller than 50 nm and within the range of 50–100 nm, accounting for 24.6 and 49.9%, respectively. In general, MIP demonstrates high measurement accuracy for pore diameter smaller than 200 nm with significant pore volume shown in Fig. 5d. In comparison, the total porosity in three dimensions measured by X-CT is evaluated in Table B2. The results reveal that SC3 has higher porosity than SL3 when the pore diameter is smaller than 200 nm, which is consistent with MIP analysis. Additionally, X-CT enables quantitative characterization of larger pores, further revealing that SL3 exhibits higher total porosity than SC3 (Table B2) due to the introduction of entrapped air and inhomogeneous distribution of CSFs [11].

The fractal analysis results of GSCs characterized by NAD and MIP s are illustrated in Fig. B1. According to the relationship between N_2 adsorption force and the related distance from the adsorption medium, Frenkel, Halsey, and Hill proposed a multimolecular layer gas absorption model (FFH model) [55], as expressed in Eq. ((− ln(P/P0)) + C 4):

$$In(Q) = k\ln(-In(P/P_0)) + C \tag{3}$$

where Q is the amount of N_2 adsorption (cm^3/g), P is the adsorbed equilibrium pressure (MPa), P_0 is N_2 saturated vapor pressure (MPa), and k and C are the slope and constant determined by the linear regression fitting of $\ln(Q)$ as a function of $\ln(-\ln(P/P_0))$. Avnir et al. [56] and Pfeifer et al. [55, 57] further optimized the calculation formula of fractal dimension (Eqs. 4–6) based on capillary condensation and surface tension.

$$k = (D_N - 3)/3 \tag{4}$$

$$k = D_N - 3 \tag{5}$$

$$\delta = 3(1 + k) - 2 \tag{6}$$

Here, δ is used to characterize whether surface tension is the dominant force in adsorption. When $\delta > 0$, surface tension can be ignored, and D_N can be calculated by Eq. (4); when $\delta < 0$, surface tension is the main adsorption force, and D_N can be calculated by Eq. (5).

Based on MIP results, the pore fractal dimension for macro pores can be calculated using Menger sponge model [58, 59], as expressed in Eqs. (7)–(8):

$$InVp = (3 - D_m)In(P' - Pt) + InC1 \tag{7}$$

$$D_M = 3 - k_1 \tag{8}$$

where V_p is the cumulative pore volume (cm^3), P' is the pressure (MPa), P_t is the pressure above threshold (MPa), and k_1 and $\ln C_1$ are the slope and constant determined by the linear regression fitting of $\ln V_p$ as a function of $\ln(P' - P_t)$.

Although the extensive pore network within GSCs is composed by multiple pores, it is hard to realize the comprehensive characterization of this multiscale pore structure. Following the fractal results of GSCs derived from NAD and MIP in Fig. B1, quantification of mesopore and

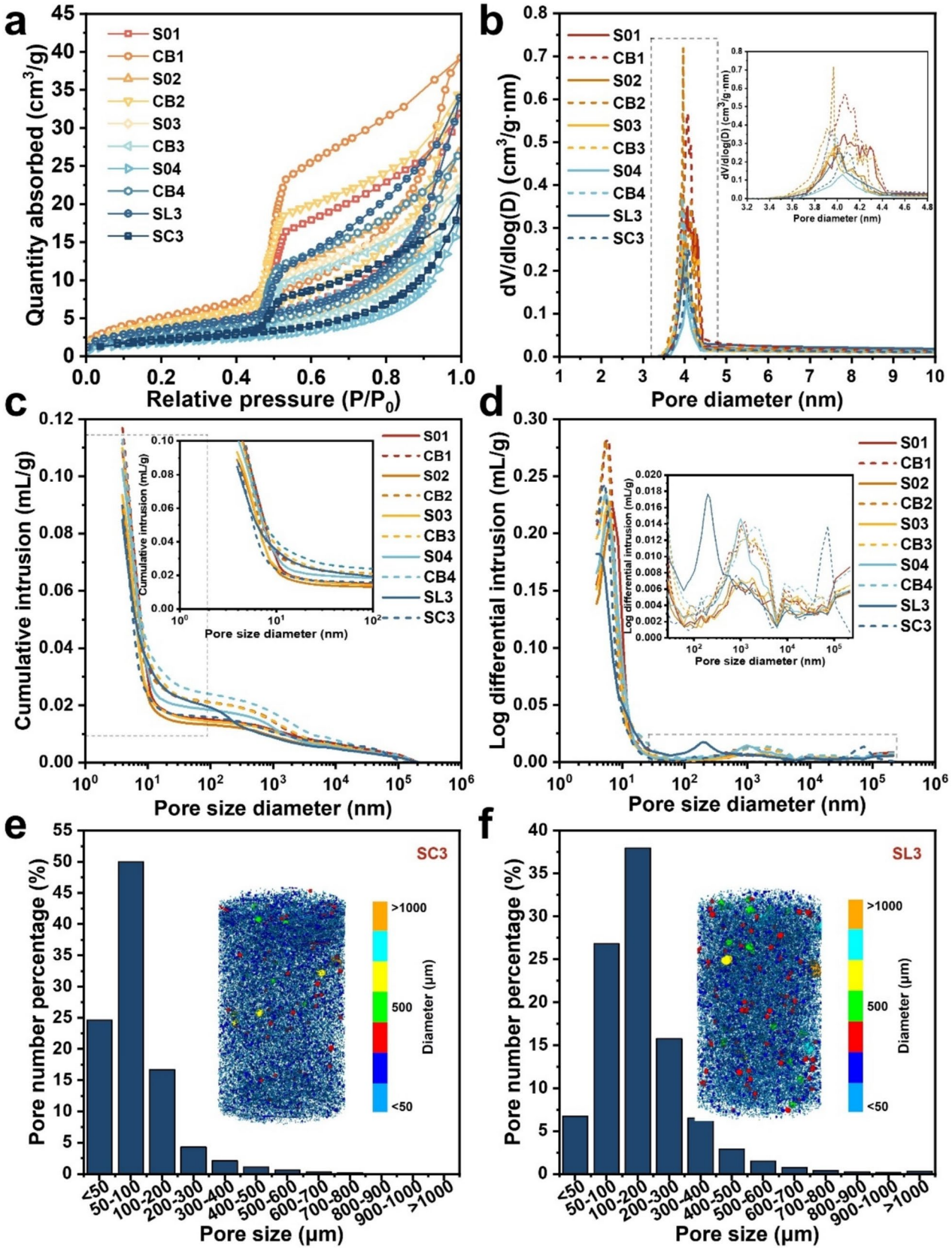

Fig. 5 Pore structure characterization of GSCs as determined by different methods: (a, b) NAD; (c, d) MIP; (e, f) X-CT

macropore fractal dimensions can be quantified. Considering the relationship between pore fractal dimension and pore volume distribution described by FHH and Menger sponge models, multiscale synthetic fractal dimension (D_c) for porous GSCs can be further calculated by weighted average with the proportion of pore volume in different pore size as expressed in Eq. (10):

$$D_c = A_{Ni}\sum_{i=1}^{n} D_{Ni}b_{Ni} + B_{Mi}\sum_{j=1}^{m} D_{Mi}b_{Mi} \quad (9)$$

where A_{Ni} represents the proportion of micropore volume to total pore volume (%); D_{Ni} represents the fractal dimension of the i-th pore size segment in the micropore stage; b_{Ni} represents the ratio of the pore volume of the i-th pore size segment in the micropore stage to the total pore volume of the micropores (%); B_{Mi} represents the proportion of macropore volume to total pore volume (%); D_{Mi} represents the fractal dimension of the i-th pore size segment in the macropore stage; b_{Mi} represents the ratio of the pore volume of the i-th pore size segment in the micropore stage to the total pore volume of the micropores (%).

Table 4 summarizes fractal analysis results of meso-, macro-, and multiscale pore fractal dimensions of GSCs. The value of fractal dimension is inversely proportional to the distribution of the pore structure. It is clear from Table 4 and Fig. B1 that the addition of single NCB and CSF leads to an increase in the fractal dimension of micropore by using FHH model and reduction of the fractal results on the macropores. Notably, the minimum fractal dimension is obtained for GSCs containing hybrid NCB and CSF with micropores. The fractal dimension of SC3 is 1.716, which decreases by 2.39% for S03, 2.56% for CB3, and 5.92% for SL3. This reduction leads to a more uniform mesopore distribution and significantly enhanced connectivity, while having an adverse effect on the macropores and multiscale pores.

3.3.2 Interface microstructure

Figure 6a–d demonstrate SEM images of the interface between GSC matrix and CSF. Both SL3 and SC3 exhibit compact interfacial bonding between CSF and geopolymerization products. The presence of nano-C-(A)-S–H and C-(K)-A-S–H and K-A-S–H gels enhances the compactness and homogeneity of the fiber–matrix bond interface. As seen in Fig. 6a and b, CSF is tightly wrapped by geopolymerization products, with silicon enrichment from the activator enhancing interfacial adhesion through the formation of a silicon-rich nanogel structure. As for SC3, CSFs within the studied zone are pulled out, wherein fiber debonding and extraction behaviors contribute to the pronounced flexural strength and fracture energy (Fig. 3).

Figure 6e and f present interfacial characterization through SEM image in BSE model and EDS linear mapping. There is no porous and weak transition zone around the aggregate, which is different from that of OPC-based concrete [60]. The matrix between CSF and aggregate is compact and uniform due to homogeneous Ca, Si, and Al element distribution. The dissolution and reaction of Ca, Si, and Al that originated from aluminosilicate precursors in the highly alkaline environment promoted the formation of high-strength C-A-S–H, K-A-S–H, and C-(K)-A-S–H nanogel phases [61]. The rich elemental concentrations in Fig. 6g further verify the presence of these highly disordered nanogel phases. On the other hand, NCB particles with nanodiameters are responsible for refining pore structure, and filling the nanovoids in the porous regions and microcracks within the interface. As illustrated in Fig. 6g, the distribution of carbon element demonstrates that NCB particles are evenly distributed within the nanostructure of the matrixes, despite the local agglomeration of NCB in the upper left region. They are wrapped by geopolymerization products acting as nucleation sites for nanogel formation and thereby optimizing the distribution of geopolymerization products

Table 4 Fractal analysis results in meso-, macro-, and multiscale pore fractal dimension

Mixtures	NAD						MIP		MD			
	k	C	R^2	δ	D_N	$k1$	ln$C1$	R^2	D_M	A_N	B_M	D_c
S01	− 1.251	6.02	0.97015	− 2.753	1.749	0.218	− 5.85	0.89285	2.782	14.29	85.71	2.634
CB1	− 1.161	5.61	0.95627	− 2.483	1.839	0.299	− 6.40	0.90757	2.701	17.32	82.68	2.552
S02	− 1.175	6.30	0.96592	− 2.525	1.825	0.240	− 6.21	0.91352	2.760	13.79	86.21	2.631
CB2	− 1.145	5.74	0.94569	− 2.435	1.855	0.278	− 6.17	0.91110	2.722	14.02	85.98	2.600
S03	− 1.242	6.33	0.96888	− 2.726	1.758	0.234	− 6.04	0.90976	2.766	10.55	89.45	2.660
CB3	− 1.239	6.30	0.97053	− 2.717	1.761	0.296	− 5.95	0.91336	2.704	9.30	90.70	2.616
S04	− 1.269	6.90	0.95258	− 2.807	1.731	0.279	− 6.44	0.91868	2.721	8.00	92.00	2.642
CB4	− 1.305	6.30	0.95945	− 2.915	1.695	0.267	− 5.90	0.91868	2.733	10.27	89.73	2.626
SL3	− 1.176	6.16	0.97717	− 2.528	1.824	0.316	− 6.92	0.98827	2.684	17.90	82.10	2.530
SC3	− 1.284	6.14	0.94790	− 2.852	1.716	0.174	− 5.36	0.94092	2.826	9.02	90.98	2.726

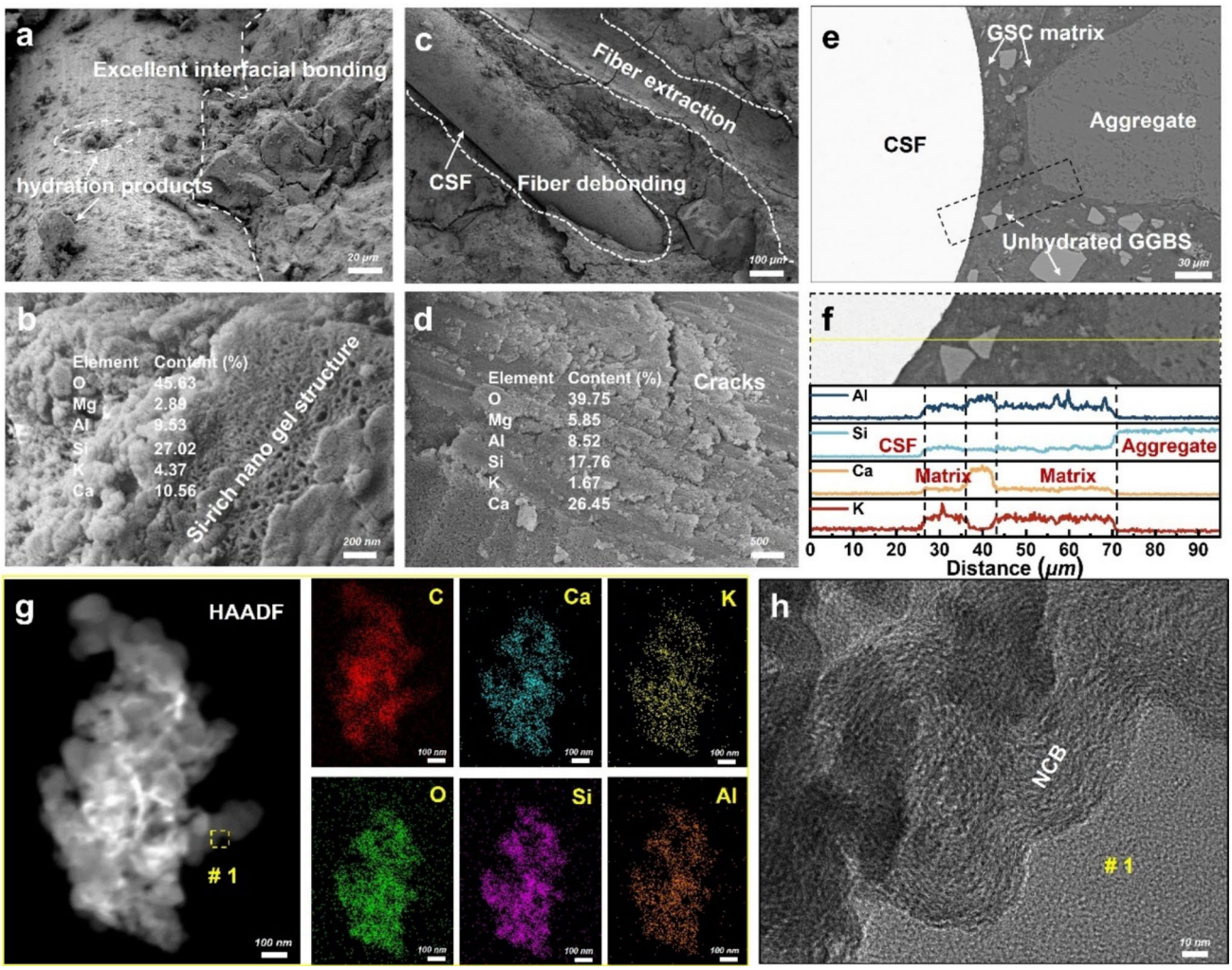

Fig. 6 Multiscale microstructure of phases in GSCs: (a) SEM image of SL3; (b) enlarged nanogel structure of (a); (c) SEM image of SC3; (d) enlarged geopolymerization product microstructure of (c); (e) SEM image in BSE model of SC3; (f) line scanning profile across the zoon of (e); (g) TEM and the corresponding elemental mapping of geopolymerization products; (h) HRTEM image of NCB of (g)

(Fig. 6h) [62]. Consequently, the formation of nano-filling effects of NCB and calcium aluminosilicate gels contributes to the development of homogeneous and dense interfacial bonding in GSCs. These mechanisms improve interfacial stiffness and promote more uniform deformation, leading to enhancement in strength, toughness, and fracture energy [63].

4 Discussion

4.1 Self-sensing mechanisms under flexural loading

Figure 7 illustrates conductive variation of GSCs under flexural loading. Based on the above analyses, three conductance mechanisms can be proposed for GSCs incorporating NCB or/and CSFs [64, 65]: (a) ionic conduction through mobile free ions within the interconnected capillary network of the pore solution; (b) contact conduction occurring between adjacent conductive fillers, that is, NCB particles, Linear connections along CSFs, and volumetric conduction formed by the hybrid NCB and CSFs within a 3D cross-linked SiO_4 and AlO_4 tetrahedron network; (c) tunneling conduction between these closely spaced conductive fillers. At high frequencies, the electrical conductivity can be further enhanced by capacitive effects [65], primarily due to the formation of double layer capacitance at the pore wall, pore solution interface, and the conductive filler/matrix/filler network as the hydrated cations are attracted to negatively charged particles [31, 48].

The electrical response of GSCs under flexural loading is dependent on the load-carrying evolution and electrically conductive variations. As illustrated in Fig. 7, during three-point bending testing, the specimen experiences

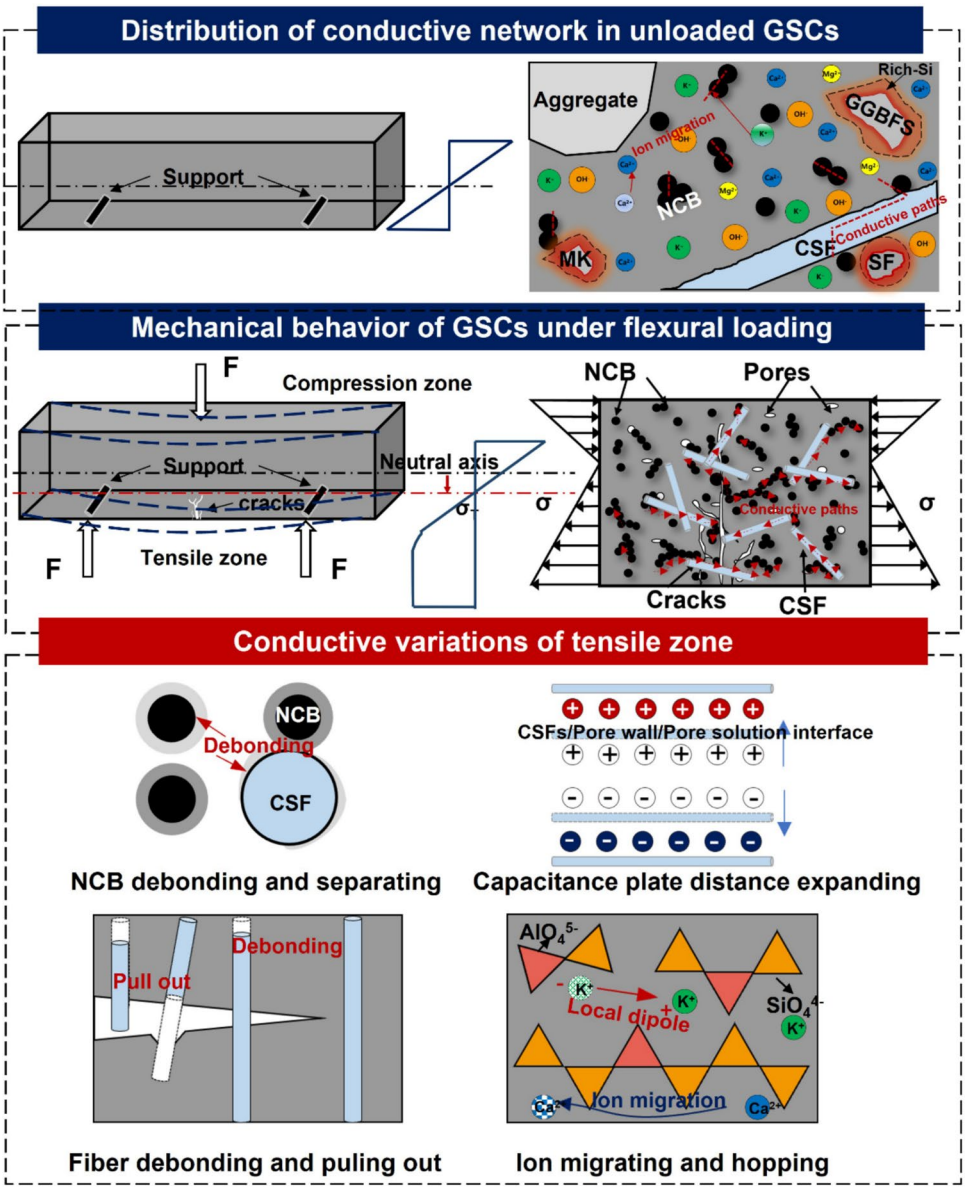

Fig. 7 Self-sensing mechanisms of GSCs under flexural loading

compression on the upper side and tension on the lower side due to the effect of the bending moment [4, 11]. During the initial elastic stage, the stress and strain distributions across the cross-section are linear with tensile and compressive stress satisfying static equilibrium conditions. Herein, conductive fillers are randomly distributed within the matrix, and the conductive network retains its pristine integrity as the applied load is insufficient to induce apparent deformation. Following progressive loading, both compressive and tensile stress increase. For the upper compression zone, the distance of conductive fillers is narrowed along the radial direction, triggering the rearrangement of conductive fillers and reconfiguration of extensive conductive network. In contrast, the conductive fillers at the lower region of the specimen are separated from the complete conductive network due to the applied tensile stress. The applied tensile stress continually increases until it attains the ultimate strength of GSCs, resulting in the initiation and propagation of cracks. In this process, the neutral axis of GSCs without fillers/with NCB shifts downward due to restricted tensile stress increase from rapid cracking in the tension zone. The specimens experience abrupt fracture when cracks fully penetrate the cross-section, resulting in complete disruption of conductive paths and consequent peak in FCR. The effects of CSFs pull-out resistance and intrinsic elastic deformation allow GSCs to sustain continuous stress and strain in the tension zone and drive the neutral axis migration toward the compression surface (Fig. 7).

The hybrid NCB and CSFs enhance the self-sensing behaviors of GSCs by improving ductility at low strain levels and

stability at high strain/stress levels. On the one hand, the incorporation of NCB refines the nanopore structure (Fig. 5) while enhancing the interfacial bonding and microstructure compactness (Fig. 6). The bridging effect of CSFs effectively inhibits the propagation of macrocracks and induces the appearance of multiple cracks, enabling plastic deformation. Moreover, NCB primarily facilitates short-range electron transport through particle-to-particle contacting and hopping, while CSFs enable long-range charge conduction through their interconnected fibrous structure [66, 67]. Their synergistic interaction establishes the extended conductive network, thereby enhancing the sensing sensitivity of GSCs. In addition, the increase of ion migration and capacitance effect also exhibit a positive correlation with the sensitivity (Fig. 7). The migration of mobile hydrated cations within the pore structure during flexure induces a charge imbalance and a local dipole [68]. The dominated alkali cations move and hop to balance the single negative charge of AlO_4 tetrahedron, while the remaining cations serve as the charge carriers [69]. The directional migration of ions generates a capacitance effect and the changes in capacitance plate distance and the relative dielectric constant caused by flexural loading leads to a change in the variation in capacitance [70]. However, when the applied stress exceeds the interfacial bond strength between CSF and matrix, the consequent fiber pull-out and NCB/fiber debonding phenomenon may directly increase contact resistivity by disrupting conductive pathway, adversely affecting the contacting conduction and tunneling conduction [14].

4.2 Optimizing the dispersion and alignment of NCB and CSFs in GSC fabrication

Apart from the microstructure analyzed in Sect. 3.3, the spatial distribution of CSF, which is responsible for the organization of mechanical and conductive reinforcement structure, plays a critical role in optimizing the self-sensing properties of GSCs. The original CSF orientation coefficient (η_θ) and dispersion coefficient (α) characterized by X-CT in 3D space (Fig. C1) can be calculated using Eqs. (10)–(12) [72, 73]:

$$\eta_a = \frac{1}{N_f}\sum_{i=1}^{N_f}\cos\theta_i \tag{10}$$

$$\eta = \sqrt{{\eta_X}^2 + {\eta_Y}^2 + {\eta_Z}^2} \tag{11}$$

$$\alpha = exp[-\sqrt{\frac{\sum(\frac{X_i}{X_a}-1)^2}{t}}] \tag{12}$$

where η_a is the orientation coefficient in one of the axes (a represents the X, Y, or Z axis), N_f is the total number of fibers, θ_i is the orientation angle between the i-th fiber and the axis (°), η is the comprehensive orientation coefficient to refine the 3D orientation factor, t is the number of CT images, X_i is the number of fibers in the i-th image, and X_a is the average of fibers. When $0.5 \le \alpha \le 1$, the fibers are evenly distributed within the Matrix; when $0 \le \alpha \le 0.5$, the fibers are unevenly distributed within the matrix.

On the other hand, CSF distribution governs the interface among the fiber–matrix, aggregate–matrix, and NCB–matrix, resulting in different flexural fracture regimes. The interfacial bond strength (τ_{fu}, MPa) between CSF and matrix can be quantified by flexural stress and CSF distribution parameters in Eq. (13) [74]:

$$\tau_{fu} = \frac{\sigma_f d}{4\alpha\lambda_c l V} \tag{13}$$

where σ_f is the flexural stress (MPa), d is the diameter of CSF (mm), λ_c is the length-related bonding coefficient with a value of η, l is the length of CSF (mm), and V is the volume content of CSF (vol.%).

Under flexural loading, crack initiation and propagation primarily exhibit mode I fracture behavior, as the tensile stress acts perpendicular to the crack plane. This crack pattern at the onset of fracture was also detected in the digital image by Lu et al. [29]. At the crack tip, the applied load is carried by the bridging CSFs, where the stress is transferring from CSFs to the uncracked matrix through shear bonding [75]. In this process, one key factor underpinning the first cracking energy (E_f, J/m^2) is the interfacial bond strength, compounded by the slipping/debonding/bridging effects and the frictional shearing resistance [45, 76]. This crack fracture mode aligns with previous observations in [45], and its quantitative characterization remains applicable to GSCs. The first cracking energy therefore can be calculated using Eqs. (14)–(18):

$$E_f = \Delta U_{f-mc} + \Delta U_{fr} + U_{db} \tag{14}$$

$$\Delta U_{f-mc} = \frac{V_{ef}}{E_G}\left[\frac{7}{48}\frac{\tau_{fu}^2 l_f^3}{d^2} - (E_G\varepsilon_{mu})^2\frac{l_f}{4}\right] \tag{15}$$

$$\Delta U_{fr} = \frac{V_{ef}\tau_{fu}l_f}{4d}\left[\frac{\tau_{fu}l_f}{3E_G d} - \frac{1}{2}\varepsilon_{mu}\right] \tag{16}$$

$$U_{db} = \frac{V_{ef}l_f G_{II}}{d} \tag{17}$$

$$G_{\Pi} = 2\Delta a G_{com} \tag{18}$$

where ΔU_{f-mc} is the crack-bridging CSFs' strain energy (J/m^2), ΔU_{fr} is the CSF–matrix fractional slip energy (J/m^2),

U_{db} is the debonding energy consumed by the elastic bond between CSFs and GSC matrix (J/m^2), V_{ef} is the effective volume fraction of fibers (vol.%) calculated following the method in [45], E_G is the elastic modulus of CSFs (E_G=200 GPa), ε_{mu} is the elastic ultimate strain ($\times 10^{-6}$), G_{II} is the fracture energy followed mode II caused by shearing failure (J/m^2) [75], G_{com} is the complementary energy derived from Fig. 3b (J/m^2), and Δa is the permissible main crack width ($\Delta a = 0.05$mm) [77].

The distribution coefficients and flexural fracture parameters of GSCs are summarized in Table 5. Although SC3 and SL3 exhibit comparable CSF orientation coefficients, the addition of NCB leads to a 159% improvement in CSF dispersion of SC3 compared to SL3. This greater dispersion accounts for the enhanced electrical conductivity (Fig. 3) and strain-sensing sensitivity (Fig. 4). Furthermore, the optimized homogeneity directly contributes to 9.25% higher interfacial bond strength compared to SL3. As shown by the crack images in Fig. D1, the crack surface of SC3 and SL3 contain CSFs, which provide bridging effect evidently. During loading, the regional matrix spalls as the crack expands and the load increases, while slip occurs due to load transfer through CSFs [78]. Particularly in SC3, another distinct crack forms when the transferred tensile stress exceeds the tensile strength. The tendency for multiple cracking patterns can be attributed to the enhanced interfacial bonding and greater flexural fracture resistance resulting from the addition of hybrid NCB and CSFs. Accordingly, the first cracking energy, fractional slip energy, and bridging CSF energy in SC3 demonstrate an increase of 2.8%, 21.8%, and 21.2%, respectively, when compared to SL3, whereas the debonding energy and shear fracture energy show substantial reduction.

Consequently, the distribution and spatial arrangement of NCB and CSFs play a pivotal role in enhancement for flexural fracture resistance and sensing properties of GSCs. Although the spatial distribution of CSFs can be thoroughly characterized, the 3D distribution of NCB remains challenging to investigate. To maximize mechanical and sensing effectiveness, the specimen preparation and filler dispersion should be well designed to ensure the homogeneous and effective distribution of NCB and CSF within the matrix. Besides focusing on the dispersing agent, there is a great potential in tailoring the CSF orientation. Aligning the CSF arrangement along the direction of the applied force is expected to enhance load-bearing capacity and continuous sensing sensitivity, making it promising to fabricate GSC for intelligent structure in the future.

Table 5 The effect of CSF distribution on the flexural fracture energy of GSCs

Mixtures	SC3	SL3
Dispersion coefficient	0.954	0.368
Orientation coefficient	0.667	0.657
Interfacial bond strength (MPa)	19.95	18.26
First cracking energy (J/m^2)	54.940	53.423
Crack-bridging fiber strain energy (J/m^2)	20.166	16.640
Fractional slip energy (J/m^2)	8.819	7.240
Debonding energy (J/m^2)	25.955	29.542
Shearing fracture energy (J/m^2)	0.316	0.365

4.3 Sustainability analyses by ecological and economic assessments

The environmental and economic performance is of great concern for the manufacture and application of GSCs. The environmental impact assessment follows the life cycle assessment framework established by the International Organization for Standardization (ISO 14075) [79]. Carbon footprint serves as the primary indicator, encompassing three critical life cycle stages: raw material production, transportation, and GSC manufacturing processes. Based on the Chinese life cycle database and relevant literature, the embodied carbon dioxide emissions for manufacturing GSCs can be evaluated by setting CO_2e/kg of GGBFS, MK, SF, PH, PS, CSFs, NCB, and QS with values of 0.083 [81], 0.122 [83], 0, 2.2 [84], 1.3 [84], 1.496 [80], 0.286 [83], and 0.033 kg [83], respectively. During the transportation stage, carbon dioxide emissions can be calculated based on transportation distance and truck fuel consumption. Given the real cases of manufacturing a GSC, it must be near/in major cities that all raw materials and market are within a reasonable distance. A good model is the practice of precast concrete plant. Therefore, the transportation distances of raw materials can be set reasonably as follows: 200 km of GGBFS, 500 km of MK, 200 km of SF, 100 km of PH, 100 km of PS, 100 km of CSFs, 500 km of NCB, and 300 km of QS. It should be noted that these distances are set according to current practice in China and must differ in different areas and countries. The impact of transportation distance is true but not that large as long as it is in a reasonable range [85]. The carbon emission factor for an 8-t diesel truck is 0.168 kg CO_2e/(t·km) [83]. The manufacturing process covers mixing and curing, and their carbon dioxide emissions can be estimated as 5.83 and 2.18 kg CO_2e/t, respectively [86].

Figure 8a–c illustrate the carbon dioxide emissions of GSCs across raw materials, transportation, and manufacturing process, with detailed data listed in Tables E1-3. Regarding raw material production emission, the utilization of activators, NCB, and CSFs accounts for the predominant proportion. Especially, the introduction of conductive fillers drastically raises the carbon emission of raw materials. For example, incorporating single NCB and CSF into a GSC mixture composed of 60% GGBFS, 25% MK, and 15% SF induce increases in total CO_2 emissions of 30.8 and

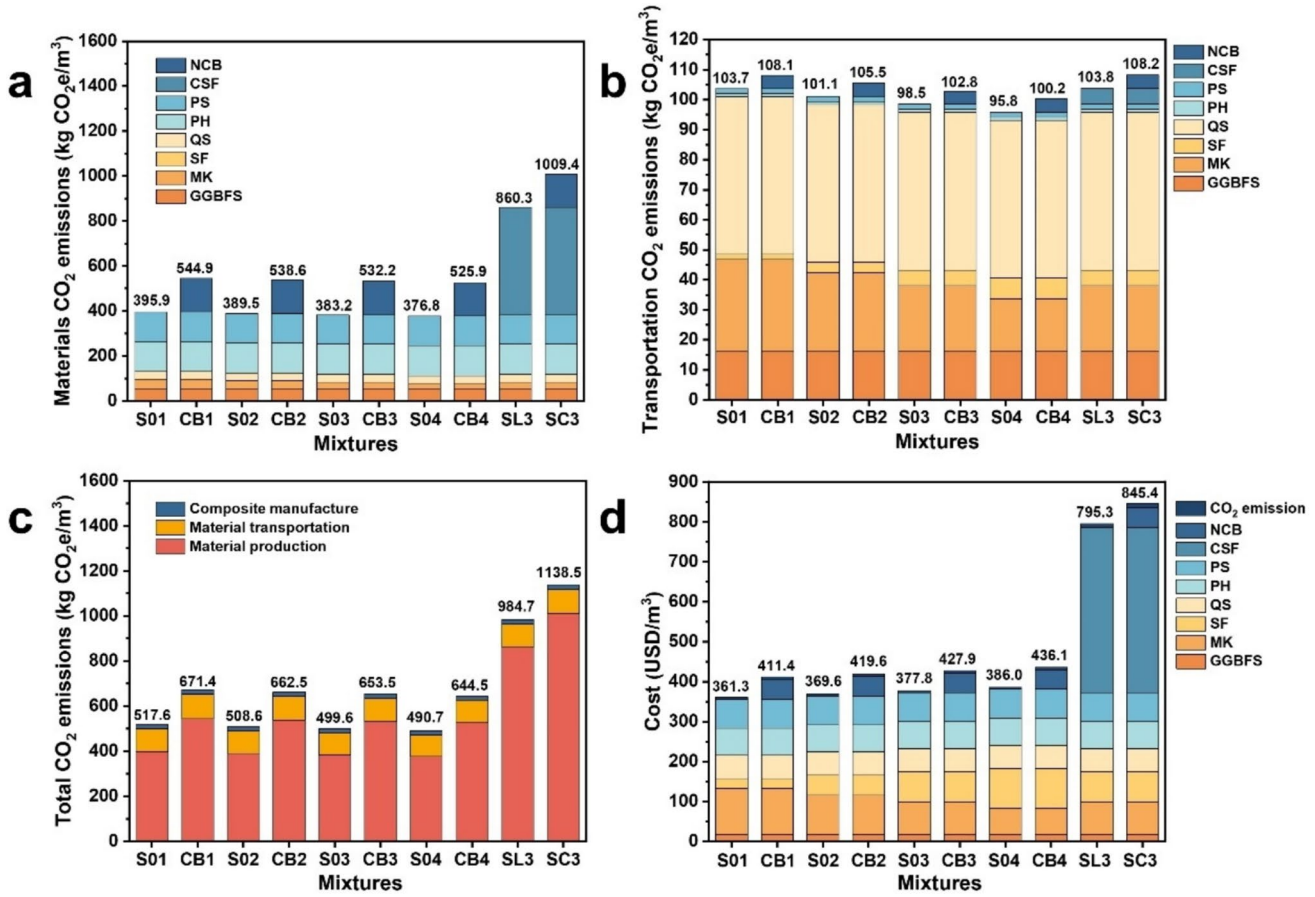

Fig. 8 The effect of mixture composition on sustainability: (a) embodied carbon dioxide emission of raw material production; (b) embodied carbon dioxide emission of raw material transportation; (c) total embodied carbon dioxide emission; (d) economic performance

97.0%, respectively. The highest total CO_2 emission reaching 1138.5 kg CO_2e/m^3 was observed when both NCB and CSF were added. Conversely, GSCs show a progressively reduced carbon footprint with increasing SF contents. This is ascribed to the fact that the precursors are industrial by-products, having substantially lower production emission compared to OPC. Locally sourced chemical activators and CSFs demonstrate significantly lower carbon footprints due to minimized transport distances.

By systematically tracking the price of raw materials, the latest market survey data indicates that the costs are 26.8 USD/t for GGBFS, 317.02 USD/t for MK, 478.4 USD/t for SF, 965.5 USD/t for PH, 720.5 USD/t for PS, 1296.9 USD/t for CSFs, 936.7 USD/t for NCB, and 64.8 USD/t for QS. The total cost shown in Fig. 8d and Table E4 is evaluated following the study of [82]. It should be noted that the economic performance of GSCs is influenced by the practical production costs and related carbon emission. Apart from the alkaline activators, the addition of SF and CSFs leads to a reverse effect due to its higher cost. Compared to GSCs without fillers, the cost increases by 110.5 and 123.8% with the addition of single CSF and hybrid NCB and CSF, respectively.

In conclusion, GSCs reinforced with hybrid NCB and CSFs provide a highly cost-effective solution for SHM, achieving a satisfying balance among carbon emissions, mechanical strength, and sensing sensitivity. Future investigation is worthwhile to explore the feasibility of incorporating recyclable and replaceable cementitious materials, recycled conductive fillers, and alternative cheap activators, without comprising their environmental, structural, and intelligent performance.

4.4 Challenges and pathways forward

The development and practical application of GSCs face some challenges though, particularly in terms of mixture formulation and preparation complexity. It is advantageous that geopolymer manufacturing could use a wide range of aluminosilicate precursors, such as the GGBFS and SF used in this study, while it also raises an issue of vibration in composition of differently sourced materials. This means the suitability of each precursor should be examined by a

whole set of testing, including the basic reactivity and the impacts on conductivity and mechanical properties. In this study, we provide an empirical formulation, but the exact conductivity and sensitivity should change when other materials are used. Secondly, the current manufacturing process adopts the pre-mixing method of alkaline activator, which is a common way of producing geopolymer binders. This is not friendly in construction industry when staff are required to follow strict chemistry procedures for safety. Recent breakthroughs, such as the one-part geopolymer technology and single-component GSC [65], offer promising solutions by enabling simplified preparation through direct water mixing. This requires a mature supply chain of geopolymer materials, which is still nascent in many areas of the world. It is also acknowledged that despite the advance of this study, research gaps remain that require more systematic investigation, including performance optimization by finer adjustment of quantity of mixture components, long-term durability validation, and the establishment of standardized application protocols, particularly focusing on scalable production methods, cost control, and field implementation techniques to facilitate broad industrial adoption.

5 Conclusions

This study systematically investigated the effects of precursors, NCB, and CSFs on mechanical, electrical, and self-sensing properties of GSCs, with a deep exploration in the enhancement of hybrid NCB and CSF-reinforced GSCs to maximize the structural and functional performance. The optimal aluminosilicate precursor composition for high strength and conductivity of GSCs is identified as 25–30% MK and 10–25% SF, with CaO/SiO_2, CaO/Al_2O_3, and SiO_2/Al_2O_3 ratios of 0.49–0.53, 0.80–0.90, and 1.50–1.80, respectively. GSCs reinforced by hybrid NCB and CSF exhibit high cost-effectiveness, achieving enhancement in fracture resistance (first cracking energy of 54.9 J/m^2), electrical conductivity (28-day AC resistivity of 150.6 Ω·m), and sensing sensitivity (*GF* of 3853.4 at first-crack initiation). This multi-objective optimization originates from the synergistic effects of hybrid NCB-CSF system within the 3D cross-linked SiO_4 and AlO_4 tetrahedron network, including the contribution of refined nanopore structure, geometrically optimized CSF distribution, and densified interface microstructure with nanogel formation. The hybrid NCB and CSF reinforced GSCs in this study demonstrate significant potential for SHM in intelligent structure. However, their large-scale application faces three critical manufacturing challenges in optimizing conductive fillers' spatial distribution, employing more low-carbon substitutes and developing recyclable and replaceable materials, which requires extensive attention in future investigations.

Supplementary Information The online version contains supplementary material available at https://doi.org/10.1007/s42114-025-01462-3.

Acknowledgements Authors acknowledge the Experimental Center of Materials Science and Engineering in Tongji University.

Author Contribution D. W. conceived and designed the project, wrote the main manuscript; S. D., C. N. and C. S. conducted data collection, data analyses and manuscript preparation; X. L. and Q. R. conducted investigation and visualization; Z. J. and Z. Z. revised the manuscript, methodology, review, and supervised this study.

Funding This work was supported by the National Natural Science Foundation of China (52378257 and U2001225), Fundamental Research Funds for the Central Universities (22120230174), Open Funds of Ningbo Institute of Materials Technology and Engineering, Chinese Academy of Sciences (2024K08), and the Science and Technology Program of Jiaxing, Zhejiang Province (2023AY11039). This work was also supported by Geopoly ® (Shanghai, China).

Data Availability Data will be made available on request.

Declarations

Competing Interests The authors declare no competing interests.

References

1. Purbayanto MAK, Presser V, Skarżyński K et al (2025) MXenes: multifunctional materials for the smart cities of tomorrow. Adv Funct Mater 35:2409953. https://doi.org/10.1002/adfm.202409953
2. Ra Y, You I, Kim M et al (2021) Toward smart net zero energy structures: development of cement-based structural energy material for contact electrification driven energy harvesting and storage. Nano Energy 89:106389. https://doi.org/10.1016/j.nanoen.2021.106389
3. Jin P, Kohestanian M, Hasany M et al (2025) Multifunctional cement-based composite with advanced self-sensing, electrothermal, and electrochemical properties. Adv Funct Mater 35:2411878. https://doi.org/10.1002/adfm.202411878
4. Dong W, Peng S, Wang K et al (2025) Integrated triboelectric self-powering and piezoresistive self-sensing cementitious composites for intelligent civil infrastructure. Nano Energy 135:110656. https://doi.org/10.1016/j.nanoen.2025.110656
5. Hao H, Bi K, Chen W et al (2023) Towards next generation design of sustainable, durable, multi-hazard resistant, resilient, and smart

civil engineering structures. Eng Struct 277:115477. https://doi.org/10.1016/j.engstruct.2022.115477
6. Chen S, Xiao H, Tian W et al (2024) New insights into strain evolution of concrete under different freeze-thaw conditions: investigation based on real-time and full-field monitoring. Cem Concr Res 178:107443. https://doi.org/10.1016/j.cemconres.2024.107443
7. Ju M, Dou ZS, Li JW et al (2023) Piezoelectric materials and sensors for structural health monitoring: fundamental aspects, current status, and future perspectives. Sensors 23(1):543. https://doi.org/10.3390/s23010543
8. Duan LY, D'Hooge DR, Cardon L (2020) Recent progress on flexible and stretchable piezoresistive strain sensors: from design to application. Prog Mater Sci 114:100617. https://doi.org/10.1016/j.pmatsci.2019.100617
9. Pang B, Jin Z, Zhang Y et al (2022) Ultraductile cementitious structural health monitoring coating: waterborne polymer biomimetic muscle and polyhedral oligomeric silsesquioxane-assisted C-S-H dispersion. Adv Funct Mater 32:2208676. https://doi.org/10.1002/adfm.202208676
10. Han B, Ding S, Yu X (2015) Intrinsic self-sensing concrete and structures: a review. Measurement 59:110–128. https://doi.org/10.1016/j.measurement.2014.09.048
11. Wang D, Dong S, Wang X et al (2022) Sensing performances of hybrid steel wires and fibers reinforced ultra-high performance concrete for in-situ monitoring of infrastructures. J Build Eng 58:105022. https://doi.org/10.1016/j.jobe.2022.105022
12. Zhang P, Gao Z, Wang J et al (2020) Properties of fresh and hardened fly ash/slag based geopolymer concrete: a review. J Clean Prod 270:122389. https://doi.org/10.1016/j.jclepro.2020.122389
13. Bajpai R, Choudhary K, Srivastava A et al (2020) Environmental impact assessment of fly ash and silica fume based geopolymer concrete. J Clean Prod 254:120147. https://doi.org/10.1016/j.jclepro.2020.120147
14. Wang D, Zhang Z, Zhu Y et al (2025) Next-generation green intelligent self-sensing geopolymer composites for enhancing construction security and sustainability: a review. Compos Part B Eng 295:112191. https://doi.org/10.1016/j.compositesb.2025.112191
15. Liu Z, Lv C, Wang F et al (2023) Recent advances in carbonatable binders. Cem Concr Res 173:107286. https://doi.org/10.1016/j.cemconres.2023.107286
16. Meyer C (2009) The greening of the concrete industry. Cem Concr Compos 31:601–605. https://doi.org/10.1016/j.cemconcomp.2008.12.010
17. Provis JL, Bernal SA (2014) Geopolymers and related alkali-activated materials. Annu Rev Mater Res 44:299–327. https://doi.org/10.1146/annurev-matsci-070813-113515
18. Qu X, Guo T, Cai J et al (2025) Characterization and analysis of electrothermal, thermoelectric, and current discharge properties of alkali-activated materials: implications for energy conversion. Cem Concr Compos 159:105987. https://doi.org/10.1016/j.cemconcomp.2025.105987
19. Wang D, Zhang Z, Ding S et al (2025) Nano-structure and sensitivity of self-sensing geopolymer composites containing nano carbon black. Cem Concr Compos 160:106072. https://doi.org/10.1016/j.cemconcomp.2025.106072
20. Kumar Sinha A, Talukdar S (2023) Mechanical and bond behaviour of high volume ultrafine-slag blended fly ash based alkali activated concrete. Constr Build Mater 383:131368. https://doi.org/10.1016/j.conbuildmat.2023.131368
21. Li C, Sun H, Li L (2010) A review: the comparison between alkali-activated slag (Si+Ca) and metakaolin (Si+Al) cements. Cem Concr Res 40:1341–1349. https://doi.org/10.1016/j.cemconres.2010.03.020
22. White CE, Daemen LL, Hartl M et al (2015) Intrinsic differences in atomic ordering of calcium (alumino)silicate hydrates in conventional and alkali-activated cements. Cem Concr Res 67:66–73. https://doi.org/10.1016/j.cemconres.2014.08.006
23. Tumidajski PJ, Schumacher AS, Perron S et al (1996) On the relationship between porosity and electrical resistivity in cementitious systems. Cem Concr Res 26:539–544. https://doi.org/10.1016/0008-8846(96)00017-8
24. Ma Y, Li F, Xie H et al (2023) Self-sensing properties of alkali-activated materials prepared with different precursors. Constr Build Mater 409:134201. https://doi.org/10.1016/j.conbuildmat.2023.134201
25. Rovnaník P, Kusák I, Bayer P et al (2019) Comparison of electrical and self-sensing properties of Portland cement and alkali-activated slag mortars. Cem Concr Res 118:84–91. https://doi.org/10.1016/j.cemconres.2019.02.009
26. Cai J, Pan J, Li X et al (2020) Electrical resistivity of fly ash and metakaolin based geopolymers. Constr Build Mater 234:117868. https://doi.org/10.1016/j.conbuildmat.2019.117868
27. Saafi M, Tang L, Fung J et al (2014) Graphene/fly ash geopolymeric composites as self-sensing structural materials. Smart Mater Struct 23:065006. https://doi.org/10.1088/0964-1726/23/6/065006
28. Song F, Li Q, Hong C et al (2025) Overlay transition zone in concrete repair: insights into microstructural evolution and micromechanical properties. Cem Concr Res 193:107868. https://doi.org/10.1016/j.cemconres.2025.107868
29. Lu M, Xie H, Wang H et al (2025) Self-sensing properties of steel fiber reinforced-alkali-activated fly ash/slag mortar. Constr Build Mater 458:139580. https://doi.org/10.1016/j.conbuildmat.2024.139580
30. Chinese National Standard GB/T 208–2014. Standard test method for density of cement, (2014).
31. Ding S, Dong S, Ashour A et al (2019) Development of sensing concrete: principles, properties and its applications. J Appl Phys 126:241101. https://doi.org/10.1063/1.5128242
32. Ding S, Xiang Y, Ni Y-Q et al (2022) In-situ synthesizing carbon nanotubes on cement to develop self-sensing cementitious composites for smart high-speed rail infrastructures. Nano Today 43:101438. https://doi.org/10.1016/j.nantod.2022.101438
33. Wetzel A, Middendorf B (2019) Influence of silica fume on properties of fresh and hardened ultra-high performance concrete based on alkali-activated slag. Cem Concr Compos 100:53–59. https://doi.org/10.1016/j.cemconcomp.2019.03.023
34. Huang Z, Zhang Z, Shi C et al (2025) Early hydration and microstructure formation of ultra-rapid hardening alkali-activated slag cement (URHA) at presence of MgO. Cem Concr Compos 160:106057. https://doi.org/10.1016/j.cemconcomp.2025.106057
35. Li N, Shi C, Wang Q et al (2017) Composition design and performance of alkali-activated cements. Mater Struct 50:178. https://doi.org/10.1617/s11527-017-1048-0
36. Luo T, Wang Q, Fang Z (2023) Effect of graphite on the self-sensing properties of cement and alkali-activated fly ash/slag based composite cementitious materials. J Build Eng 77:107493. https://doi.org/10.1016/j.jobe.2023.107493
37. Shi C, Yu K, Zheng C et al (2025) Reaction kinetics and microstructure evolution of tuff-based geopolymers with feature properties. Cem Concr Compos 164:106249. https://doi.org/10.1016/j.cemconcomp.2025.106249
38. Dong W, Li W, Luo Z et al (2020) Structural response monitoring of concrete beam under flexural loading using smart carbon black/cement-based sensors. Smart Mater Struct 29:065001. https://doi.org/10.1088/1361-665X/ab7fef
39. Wang D, Ding S, Wang X et al (2024) Low-cost flash graphene from carbon black to reinforce cementitious composites for carbon

footprint reduction. Chem Eng J 500:156926. https://doi.org/10.1016/j.cej.2024.156926
40. Park S, Pour-Ghaz M (2018) What is the role of water in the geopolymerization of metakaolin? Constr Build Mater 182:360–370. https://doi.org/10.1016/j.conbuildmat.2018.06.073
41. Li W, Guo Y, Zhang X et al (2024) Development of self-sensing ultra-high-performance concrete using hybrid carbon black and carbon nanofibers. Cem Concr Compos 148:105466. https://doi.org/10.1016/j.cemconcomp.2024.105466
42. Luo T, Ma Y, Xie H et al (2024) Piezoresistivity of carbon fiber-reinforced alkali-activated materials: effect of fly ash microspheres and quartz sands. Constr Build Mater 425:136125. https://doi.org/10.1016/j.conbuildmat.2024.136125
43. He B, Zhu X, Zhang H et al (2025) Nano-engineering steel fiber for UHPC: implication for varying cryogenic and elevated exposure. Cem Concr Compos 156:105851. https://doi.org/10.1016/j.cemconcomp.2024.105851
44. Yoo D-Y, Banthia N, Lee J-Y et al (2018) Effect of fiber geometric property on rate dependent flexural behavior of ultra-high-performance cementitious composite. Cem Concr Compos 86:57–71. https://doi.org/10.1016/j.cemconcomp.2017.11.002
45. Dong S, Wang D, Wang X et al (2022) Optimizing flexural cracking process of ultra-high performance concrete via incorporating microscale steel wires. Cem Concr Compos 134:104830. https://doi.org/10.1016/j.cemconcomp.2022.104830
46. Liu S, Sun H, Sun L et al (2012) Effects of pH and Cl− concentration on corrosion behavior of the galvanized steel in simulated rust layer solution. Corros Sci 65:520–527. https://doi.org/10.1016/j.corsci.2012.08.056
47. Qin H, Ding S, Qiu L et al (2024) Electrical properties of ultra-high-performance concrete with various reinforcing fibers. Meas Sci Technol 35:035601. https://doi.org/10.1088/1361-6501/ad128f
48. Shakib MA, Gao Z, Candamano S et al (2023) Ion channels and electroosmosis in porous geopolymers: a novel category of low-cost memristors. Adv Funct Mater 33:2306535. https://doi.org/10.1002/adfm.202306535
49. Li W, Guan X, Shi J (2024) Electrochemical behavior of zinc in alkali-activated fly ash solution. Cem Concr Compos 146:105395. https://doi.org/10.1016/j.cemconcomp.2023.105395
50. Shi J, Ming J, Wu M (2020) Passivation and corrosion behavior of 2304 duplex stainless steel in alkali-activated slag materials. Cem Concr Compos 108:103532. https://doi.org/10.1016/j.cemconcomp.2020.103532
51. Danoglidis PA, Konsta-Gdoutos MS, Shah SP (2019) Relationship between the carbon nanotube dispersion state, electrochemical impedance and capacitance and mechanical properties of percolative nanoreinforced OPC mortars. Carbon 145:218–228. https://doi.org/10.1016/j.carbon.2018.12.088
52. Bi S, Liu M, Shen J et al (2017) Ultrahigh self-sensing performance of geopolymer nanocomposites via unique interface engineering. ACS Appl Mater Interfaces 9:12851–12858. https://doi.org/10.1021/acsami.7b00419
53. Hu H, Liu Y, Chen L et al (2025) Simultaneous enhancement of mechanical robustness and self-sensing performance in fly ash-based geopolymer nanocomposites. Compos Part A Appl Sci Manuf 194:108894. https://doi.org/10.1016/j.compositesa.2025.108894
54. Dong S, Wang X, Ashour A et al (2022) Enhancement and underlying mechanisms of stainless steel wires to fatigue properties of concrete under flexure. Cem Concr Compos 126:104372. https://doi.org/10.1016/j.cemconcomp.2021.104372
55. Pfeifer P, Obert M, Cole MW et al (1989) Fractal bet and FHH theories of adsorption: a comparative study. Proc R Soc Lond A 423:169–188. https://doi.org/10.1098/rspa.1989.0049
56. Avnir D, Jaroniec M (1989) An isotherm equation for adsorption on fractal surfaces of heterogeneous porous materials. Langmuir 5:1431–1433. https://doi.org/10.1021/la00090a032
57. Pfeifer P, Wu YJ, Cole MW et al (1989) Multilayer adsorption on a fractally rough surface. Phys Rev Lett 62:1997–2000. https://doi.org/10.1103/PhysRevLett.62.1997
58. Zhang B, Li S (1995) Determination of the surface fractal dimension for porous media by mercury porosimetry. Ind Eng Chem Res 34:1383–1386. https://doi.org/10.1021/ie00043a044
59. Xie H, Wang J, Qan P (1996) Fractal characters of micropore evolution in marbles. Phys Lett A 218:275–280. https://doi.org/10.1016/0375-9601(96)00390-8
60. Luo Z, Li W, Wang K et al (2021) Comparison on the properties of ITZs in fly ash-based geopolymer and Portland cement concretes with equivalent flowability. Cem Concr Res 143:106392. https://doi.org/10.1016/j.cemconres.2021.106392
61. Tu W, Zhang M (2024) Multiscale microstructure and micromechanical properties of alkali-activated concrete: a critical review. Cem Concr Compos 152:105664. https://doi.org/10.1016/j.cemconcomp.2024.105664
62. Li W, Dong W, Guo Y et al (2022) Advances in multifunctional cementitious composites with conductive carbon nanomaterials for smart infrastructure. Cem Concr Compos 128:104454. https://doi.org/10.1016/j.cemconcomp.2022.104454
63. Han J, Pan J, Wang X et al (2023) Conductive behavior of engineered geopolymer composite with addition of carbon fiber and nano-carbon black. Ceram Int 49:32035–32048. https://doi.org/10.1016/j.ceramint.2023.07.170
64. Dong W, Ahmed AH, Liebscher M et al (2025) Electrical resistivity and self-sensing properties of low-cement limestone calcined clay cement (LC3) mortar. Mater Des 252:113790. https://doi.org/10.1016/j.matdes.2025.113790
65. Guo Y, Qu F, Dong W et al (2025) Self-sensing performance of nanoengineered one-part alkali-activated materials-based sensors after exposure to elevated temperature. Cem Concr Compos 164:106257. https://doi.org/10.1016/j.cemconcomp.2025.106257
66. Ding S, Wang X, Qiu L et al (2023) Self-sensing cementitious composites with hierarchical carbon fiber-carbon nanotube composite fillers for crack development monitoring of a maglev girder. Small 19:2206258. https://doi.org/10.1002/smll.202206258
67. Qin H, Ding S, Ashour A et al (2024) Revolutionizing infrastructure: the evolving landscape of electricity-based multifunctional concrete from concept to practice. Prog Mater Sci 145:101310. https://doi.org/10.1016/j.pmatsci.2024.101310
68. Lamuta C, Candamano S, Crea F et al (2016) Direct piezoelectric effect in geopolymeric mortars. Mater Des 107:57–64. https://doi.org/10.1016/j.matdes.2016.05.108
69. Deng L, Ma Y, Hu J et al (2019) Preparation and piezoresistive properties of carbon fiber-reinforced alkali-activated fly ash/slag mortar. Constr Build Mater 222:738–749. https://doi.org/10.1016/j.conbuildmat.2019.06.134
70. Mei J, Yin C, Zhao Y et al (2024) Effect of calcium carbide slag on the durability of alkali-activated ground granulated blast furnace slag-fly ash cementitious system. ZKG Int 77:60–67
71. Zhang H, Sarker PK, Wang Q et al (2021) Strength and toughness of ambient-cured geopolymer concrete containing virgin and recycled fibres in mono and hybrid combinations. Constr Build Mater 304:124649. https://doi.org/10.1016/j.conbuildmat.2021.124649
72. Schönlin K (1988) Ermittlung der Orientierung, Menge und Verteilung der Fasern in faserbewehrtem Beton. Beton- Stahlbetonbau 83:168–171. https://doi.org/10.1002/best.198800280
73. Zhang H, He B, Chen W et al (2024) Investigating the influence of fibre type and content on the toughness and ductility of geopolymer mortar with acoustic emission technology. Cem Concr

Compos 147:105434. https://doi.org/10.1016/j.cemconcomp.2024.105434
74. Wang D, Zhang Z, Shi C et al (2025) Comparison study of ultra-high performance geopolymer concrete (UHPGC) and ultra-high performance concrete (UHPC): mechanical properties, durability and carbon emissions. Compos Part B Eng 3307:112903. https://doi.org/10.1016/j.compositesb.2025.112903
75. Deng Y, Zhang Z, Shi C et al (2023) Steel fiber–matrix interfacial bond in ultra-high performance concrete: a review. Engineering 22:215–232. https://doi.org/10.1016/j.eng.2021.11.019
76. Zhang H, He B, Cheng Y et al (2024) Strengthening and embrittlement effect of cryogenic temperature on fiber reinforced geopolymer composite. Cem Concr Compos 153:105727. https://doi.org/10.1016/j.cemconcomp.2024.105727
77. Bhatnagar S, Popuri A (2024) Overview of energy consumption and attributes of grinding technologies in Indian cement industry. ZKG Int 77:48–58
78. Lee SW, Kim GW, Oh T et al (2023) The microstructure and mechanical properties of cementless ultra-high-performance alkali activated concrete considering geometrical properties of steel fiber. Cem Concr Compos 142:105209. https://doi.org/10.1016/j.cemconcomp.2023.105209
79. ISO 14075:2024. Environmental management—principles and framework for social life cycle assessment, (2024).
80. Zhao J, Wang A, Zhu Y et al (2024) Manufacturing ultra-high performance geopolymer concrete (UHPGC) with activated coal gangue for both binder and aggregate. Compos Part B Eng 284:111723. https://doi.org/10.1016/j.compositesb.2024.111723
81. Disu AA, Kolay P (2025) Sustainability assessment of fly ash, lime sludge, and ground granulated blast furnace slag–based geopolymer-stabilized kaolin clay. Journal of Hazardous Toxic and Radioactive Waste 29:04024048. https://doi.org/10.1061/JHTRBP.HZENG-134
82. Chen G, Zheng D-P, Chen Y-W et al (2023) Development of high performance geopolymer concrete with waste rubber and recycle steel fiber: a study on compressive behavior, carbon emissions and economical performance. Constr Build Mater 393:131988. https://doi.org/10.1016/j.conbuildmat.2023.131988
83. Liu X, Wang H, Chen J et al (2010) Methods and basic models for establishing a Chinese life cycle reference database. J Environ Sci 30(10):2136–2144
84. Sabitha D, Dattatreya JK, Sakthivel N et al (2020) Assessment of reactivity of energy efficient high volume fly ash based geopolymers through various approaches. Sādhanā 45:178. https://doi.org/10.1007/s12046-020-01417-y
85. Zhang Z, Zhu Y, Yang T et al (2017) Conversion of local industrial wastes into greener cement through geopolymer technology: a case study of high-magnesium nickel slag. J Clean Prod 141:463–471. https://doi.org/10.1016/j.jclepro.2016.09.147
86. Zhang J, Su Y, Gao H (2025) Development of CO_2-ceramsite foam concrete: mechanical properties, microstructure and environmental benefits. Case Stud Constr Mater 23:e04957. https://doi.org/10.1016/j.cscm.2025.e04957